Evolution of the Inflow Boundary Layer of Hurricane Gilbert (1988)

GARY M. BARNES

University of Hawaii, Honolulu, Hawaii

MARK D. POWELL

NOAA/AOML/Hurricane Research Division, Miami, Florida

ABSTRACT

On 12 September 1988 the two NOAA WP-3D aircraft conducted an experiment in and around an intense, outer rainband located 175 km southeast of the center of Hurricane Gilbert. Radial–height cross sections along a constant azimuth reveal a rapid and an exceptionally large increase of the equivalent potential temperature θ_e of the inflow but in a region radially outward from the rainband. Kinematic analyses that incorporate both in situ and pseudo-dual-Doppler data illustrate that the inflow is only 2 km deep and strongly divergent prior to reaching the convective core of the band. The Doppler-derived wind fields, which compare favorably with the in situ wind fields, demonstrate that there is a radially outward or return flow directly above the inflow. Soundings show that this return flow is unusually moist despite being dominated by mesoscale descent, which contrasts the dry conditions found under the anvil of virtually all tropical mesoscale convective systems.

A one-dimensional general structure entrainment model of the inflow layer, initialized with a wind field derived from the pseudo-dual-Doppler analysis, demonstrates that the overlying return flow adds substantial energy to the inflow via entrainment. The placement of this high-θ_e layer directly above the inflow is due to the circulation associated with the rainband. Low convective available potential energy, high shear of the radial wind, and a weak cold outflow at the surface are factors that help produce the shallow return flow. The analyses demonstrate that significant spatial variations of the flux divergence of heat and moisture exist in the inflow to a tropical cyclone, the variations are closely related to the secondary circulations produced by convectively active rainbands, and these variations produce significant asymmetries of θ_e within the inflow. Rainbands of this type have thermodynamic characteristics similar to an eyewall and may be the type of rainband that evolves into a convective ring.

1. Introduction

a. Background

Tropical cyclone formation depends upon the creation of a warm core, but to produce a warm core capable of lowering the surface pressure by more than a few millibars requires significant energy transfer from the ocean. The boundary layer is the recipient of this energy and serves as the enriched fuel for the main updrafts, found in the eyewall. The relationship highlighting the importance of the increase of the mean equivalent potential temperature $(\delta\theta_e)$ of the eyewall updraft column and the reduction of sea level pressure below approximately 1000 mb (δP) was first empirically derived by Malkus and Riehl (1960) using hydrostatic arguments. Later Emanuel (1986) analytically estimated the relationship using Carnot heat engine principles, and more recently Betts and Simpson

Corresponding author address: Dr. Gary M. Barnes, University of Hawaii, 2525 Correa Road, Honolulu, HI 96822.

(1987) have refined the relationship using a hydrostatic computation. This relationship has converged to be

$$\delta P \approx -3\delta\theta_e. \qquad (1)$$

The equivalent potential temperature increase during the final 200-km run toward the eyewall is small compared to the initial energy of the tropical air that is advected toward the storm center (e.g., θ_e increases from 345 to 365 K), but the additional fluxes do serve as the crucial activation energy that allows the eyewall updraft of a hurricane to occur. Numerical simulations with no initial convective available potential energy (CAPE) can create a tropical cyclone if the fluxes from the sea reach an appropriate magnitude (Rotunno and Emanuel 1987).

While the ultimate source of nearly all the energy in the atmospheric boundary layer column is clearly the sea (Byers 1944; Malkus and Riehl 1960; Ooyama 1969), the exact process by which the transfer takes place in the inflow has been difficult to identify. Frank (1977b), Anthes and Chang (1978), Betts and Simpson (1987), and Powell (1990b) have all shown that the mixed-layer θ_e can be increased through entrain-

ment of higher potential temperature θ from above as well as fluxes through the sea surface. Betts and Simpson (1987) reexamined a trajectory analysis for the inflow into Hurricane Daisy, which was first studied by Malkus and Riehl (1960), to argue that the inflow layer could receive energy from a number of mechanisms, none of which could be ruled out given the limited observations within the storm. They stated that better datasets are needed to identify the relative importance of each mechanism and especially what processes are taking place at the top of the inflow.

Mesoscale convective systems (MCSs) have been shown to significantly modify the energy transports across the sea surface and at the top of the mixed layer. Entrainment of midlevel air in the wake of a squall line, brought into juxtaposition with the mixed layer by the subsidence in this region, usually reduces the θ_e even when θ is increasing (e.g., Zipser 1977; Nicholls and Johnson 1984; Barnes and Sieckman 1984). The large sensible and latent fluxes from the sea that occur in the wake are overwhelmed by the entrainment of midlevel dry air at the top of the growing mixed layer. Hurricane rainbands are a type of MCS that have at least a fraction of their inflow passing under the upper-level outflow and through the stratiform precipitation that is in contradistinction to most tropical MCSs (Barnes et al. 1983; Barnes and Stossmeister 1986; Powell 1990a). This is potentially limiting to rainband intensity because of the possible entrainment of lower-θ_e air into the inflow that can occur under the stratiform rain of the rainband. But what if the air directly above the inflow is not characterized by low θ_e? One purpose of this paper is to argue that such a condition can occur in a hurricane and that this condition can lead to a rapid increase of θ_e in the inflow to the hurricane's inner core.

Early aircraft research on tropical cyclones emphasized building a statistically significant dataset at a few levels (e.g., 1500 and 3000 m) to identify the vortex-scale features occupying the midtroposphere. However, to identify the dominant processes that affect the evolution of the boundary layer, we need to sample the lowest 1–2 km of the atmosphere more frequently. In the decade following 1980 a series of experiments were designed to determine the pertinent physical fields associated with convectively active rainbands. These efforts concentrated resources in the boundary layer and provided the opportunity to learn how rainbands affect the energy of the inflow and thus may inhibit storm intensity (e.g., Barnes et al. 1983; Powell 1990b). These same experiments also can be used to explore the evolution of the inflow *prior* to its ascent in a rainband or the eyewall.

b. Goals

We wish to examine the evolution of the inflow of Hurricane Gilbert for 12 September 1988. We shall use the aircraft passes normal to the major axis of a long-

lived, convectively active rainband to develop mesoscale thermodynamic fields that are aligned along a constant azimuth with respect to the storm circulation center. The in situ wind observations from these passes and the Doppler radar winds obtained from the "L"-shaped flight patterns will enable us to create a three-dimensional wind field for the region adjacent to and radially outward from the band. These observations will then be used to initialize a one-dimensional general structure entrainment model similar to that used by Powell (1990b). The simulation will provide a first-order estimate of the magnitude of the heat and moisture fluxes at the top and base of the inflow layer. More importantly, the analyses will allow determination of the role the rainband circulation plays in the evolution of the inflow layer to the tropical cyclone. We hypothesize that rainbands operating in certain environments can contribute to the intensification of the hurricane by modulating the inflow boundary layer to the inner core.

2. Data and analysis techniques

a. Sampling strategy

The two NOAA WP-3Ds, *NOAA-42* and *NOAA-43*, completed four deployment strategies that are the building blocks of the rainband experiment. These include the following:

1) soundings radially inward and outward of the rainband to obtain environmental convective available potential energy (CAPE) and wind shear;

2) boundary layer soundings on either side of the band that supply a detailed view of the lowest 1000 m;

3) passes normal to the major axis of the band that are used to manufacture a mesoscale cross section of the band as a function of radial distance;

4) box patterns centered on the passes made normal to the rainband. Any two adjacent flight legs of the box (an "L") are used to obtain a three dimensional wind analysis using the pseudo-dual-Doppler technique.

The aircraft also dropped Omega dropwindsondes (ODWs) during the experiment to supplement the aircraft soundings. A total of 19 passes normal to the major axis of the band were completed at 300 (3 passes), 450 (7), 700 (3), and 1500 (6) m. Passes were at least 60 km long and occasionally as long as 120 km when flying normal to the band axis. Passes parallel to the band, which were made by *NOAA-42* flying the Doppler box patterns, were 80 km long.

b. Data treatment

The pseudo-dual-Doppler technique, so-called because one airborne radar tries to emulate ground-based radars, has produced airflow depictions of regions filled with stratiform rain (e.g., Jorgensen et al. 1983), the inner core of a tropical cyclone (e.g., Marks and Houze 1984, 1987), and large cumulonimbi (e.g., Hildebrand

and Mueller 1985; Barnes et al. 1991). All these papers supply information on the compromising aspects inherent to the technique, while Carbone et al. (1980) provide a discussion of the general limitations of Doppler radar. The most serious impediments to an accurate analysis include the determination of the airflow at the boundaries of the target volume, the length of time it takes to complete the Doppler "L" pattern, and the horizontal resolution of the airborne system. "Sea clutter" at the base of the volume and a lack of scatterers near the volume top are the chief causes of poor boundary condition determination. The radar samples one wind component normal to the aircraft track during the first leg of the "L" and the other component on the second leg. For the combination to be meaningful the target volume must be steady and move with a steady motion. Obviously, short scan times are necessary to resolve convective-scale features that have a lifetime on the order of minutes. The spin rate of the antenna, range to the target volume, beamwidth, and aircraft ground speed all combine to limit the horizontal sampling resolution to 1 km and the potential for significant aliasing problems for targets with dimensions less than 3–4 km.

The Doppler data obtained in Gilbert are processed in the manner described by Marks and Houze (1984) and Barnes et al. (1991). Our interest is to determine the mesoscale inflow and outflow characteristics for the area adjoining the band, not the convective-scale features within the band. More details particular to the volume of interest for this study will be presented with the results.

The in situ data are treated similarly to Barnes and Stossmeister (1986), with the 1-Hz flight level data smoothed by a running mean filter that preserves scales of 2 km or greater. Passes with opposite headings were used to detect any bias of the winds due to aircraft heading. Position errors are present because of the Schuler oscillation and long-term drift in the inertial navigation system (Fankhauser et al. 1985). We have used common targets as seen by each aircraft's lower fuselage radar to correct the relative position to within 2–3 km of each other. The sensor wetting correction schemes follow that described by Barnes et al. (1991), whereby the CO_2 radiometer is used to measure the temperature in-cloud, and the absolute value of the radiometer is corrected for each pass using the more reliable Rosemount thermistor when the aircraft is clear of cloud and rain. The dewpoint sensor is constrained to be less than or equal to the corrected radiometer.

Interpretation of the vertical velocity requires a correction to eliminate any biases. To do this we assume that the average vertical velocity for the ferry out to the storm, after removal of any convective-scale events, is zero. The error from this assumption will be no larger than a large synoptic-scale value of subsidence or lifting (e.g., 0.05 m s^{-1}) that we may have incorrectly eliminated. We believe that detection of strong mesoscale updrafts and subsidence zones, as well as convective-scale drafts and cores, is feasible with this scheme.

A full list of the sensors on the two WP-3Ds may be found in the 1994 Hurricane Field Program Plan (Marks and Friedman 1994; available from NOAA/AOML/HRD).

c. Coordinate system

The eye of Gilbert was over the rugged island of Jamaica during the experiment so we were not able to estimate the location and motion of the circulation center with in situ winds. In lieu of this method we have used the lower fuselage radar to estimate the center of the hurricane and assume that this fix is close to the actual circulation center. Errors in the location of the center can have a significant effect on the relative strengths of the tangential and radial winds near the eyewall but not at distances beyond 150 km from the center, where our focus lies.

A cylindrical coordinate system is chosen to identify the primary (tangential) and secondary (radial) flows relative to a fixed point on the earth's surface. Subtraction of the storm's motion from this earth-relative system provides us with the tangential (V_T, positive is cyclonic) and radial (V_R, positive is flow away from the center) flows relative to the storm center. Storm relative motions will be presented throughout this study. Both aircraft yield a direction and speed of 298° at 8.0 m s^{-1} for the hurricane based on lower fuselage scans of the inner core. We purposely decline the selection of a coordinate system that focuses on the rainband alone since we want to assess how the rainband circulation may affect flow to the inner core of the hurricane.

3. Weather situation

Lawrence and Gross (1989) review the formation, track, and behavior of Hurricane Gilbert, which became the strongest hurricane on record in the Caribbean. The storm developed from an easterly wave that was first detected on 3 September near the African coast; one week later on 10 September Gilbert achieved hurricane intensity approximately 450 km southeast of San Juan, Puerto Rico. The direction and speed that we have estimated for the hurricane (298° at 8.0 m s^{-1}) agrees well with the longer-term storm motion reported by Lawrence and Gross (1989). The best estimate of minimum sea level pressure (MSLP) as a function of time shows the hurricane deepened from 962 to 888 hPa in the 24 h after the center cleared Jamaica (Fig. 1). The aircraft did not fly into the eye but an estimated MSLP from surface and satellite data during the rainband experiment is 965 hPa. Maximum sustained winds sampled by the aircraft when the storm was at its deepest phase, late on 13 September when the hurricane was
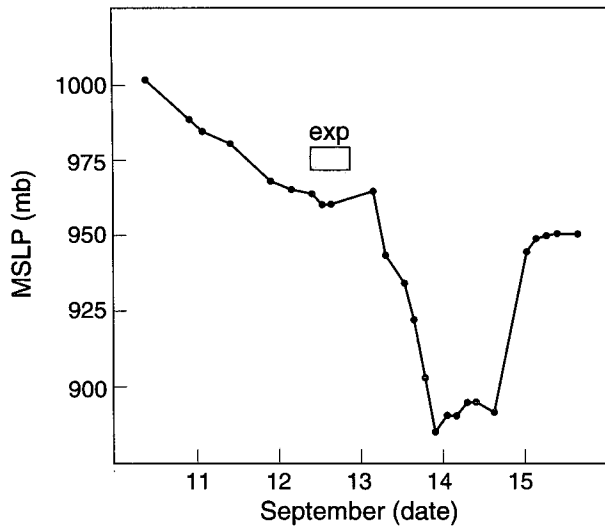
FIG. 1. Minimum sea level pressure found in Hurricane Gilbert from 8 to 15 September 1988. Period of the experiment is marked.

near the Yucatan Peninsula, was 89 m s^{-1}. The hurricane has been classified by Willoughby et al. (1989) as a concentric system wherein an outer rainband contracts and eventually evolves into the eyewall for the storm. This concentric structure was apparent on 13 September.

4. Results—Observations

a. Reflectivity structure

Most of the lower fuselage radar views (C band) of the hurricane are of the southeastern quadrant (Fig. 2). Just south of Jamaica is the eyewall, and another 100-km radial distance beyond the eyewall is the beginning of the rainband complex. One can see evidence for at least two bands that are nearly parallel to each other if the high-reflectivity regions are linked along the azimuthal direction. In this figure, the track of NOAA-43 is shown, which flew normal to the major axis of the outer band along headings of 130° and its reciprocal, 310°. NOAA-43 always samples the outer band and occasionally intercepts the inner band.

The reflectivity field, as observed with the lower fuselage radar from NOAA-43, undergoes considerable change through the experimental period. In Fig. 3a there is a narrow region of high reflectivity about 150 km long that we label the major axis of the band. Approximately 30 km to the west-northwest a second weaker band can be seen that is not as continuous in the azimuthal direction. One hour later (Fig. 3b) the inner band has strengthened, but the outer band is still the primary feature. Little band motion is obvious between these two times. Later, the inner band continues to strengthen (Fig. 3c) and toward the end of the experimental period (Fig. 3d) the inner band rivals the

older, outer band in both numbers of cells and maximum reflectivities. By this stage the inner band contains the strongest horizontal gradients of radial wind and θ_e, as well as the most sharply defined reflectivity field. Stratiform rain can be seen on either side of the band. The appearance or disappearance of these lighter, more homogeneous rain regions (contrast Fig. 3a with Fig. 3c) is correlated with the side of the band axis the aircraft is on. Enhanced attenuation caused by rain at the aircraft and by the intense cells along the band axis and beamwidth change that is a function of the distance between the aircraft and a given reflectivity feature are the primary factors for the fluctuating intensity from scan to scan. There is, in general, much less stratiform rain found radially inward of the major axis of the band. Scrutiny of the bands over 10-min periods (not shown) reveals occasional radical changes in the shape and intensity of the band, but these are largely a function of the aforementioned problems and not due to actual evolution.

Perusal of the complete set of scans from NOAA-43 and NOAA-42 shows that the original, outer band moves outward at 3–4 m s^{-1} during its mature phase, then weakens and slows, and is finally overtaken by the more robust inner band, which apparently mimics the behavior of the first band. These rainbands exhibit an evolution that differs from what has been witnessed in other hurricanes (e.g., Barnes et al. 1983; Barnes and Stossmeister 1986; Powell 1990a). These studies did not observe a new band forming radially inward of the
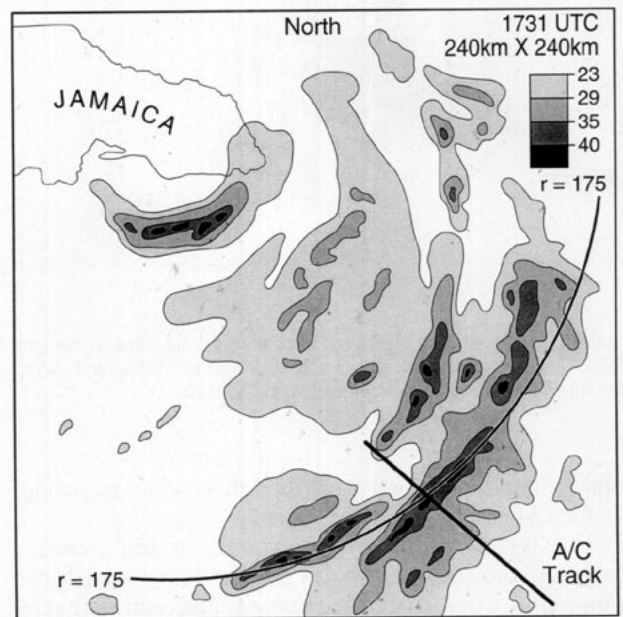

FIG. 2. A lower fuselage radar view of the storm at 1731 UTC from NOAA-43. The bold line depicts NOAA-43's mean track for the passes normal to the major axis of the band. Reflectivity levels are 23, 29, 35, and greater than 40 dBZ.
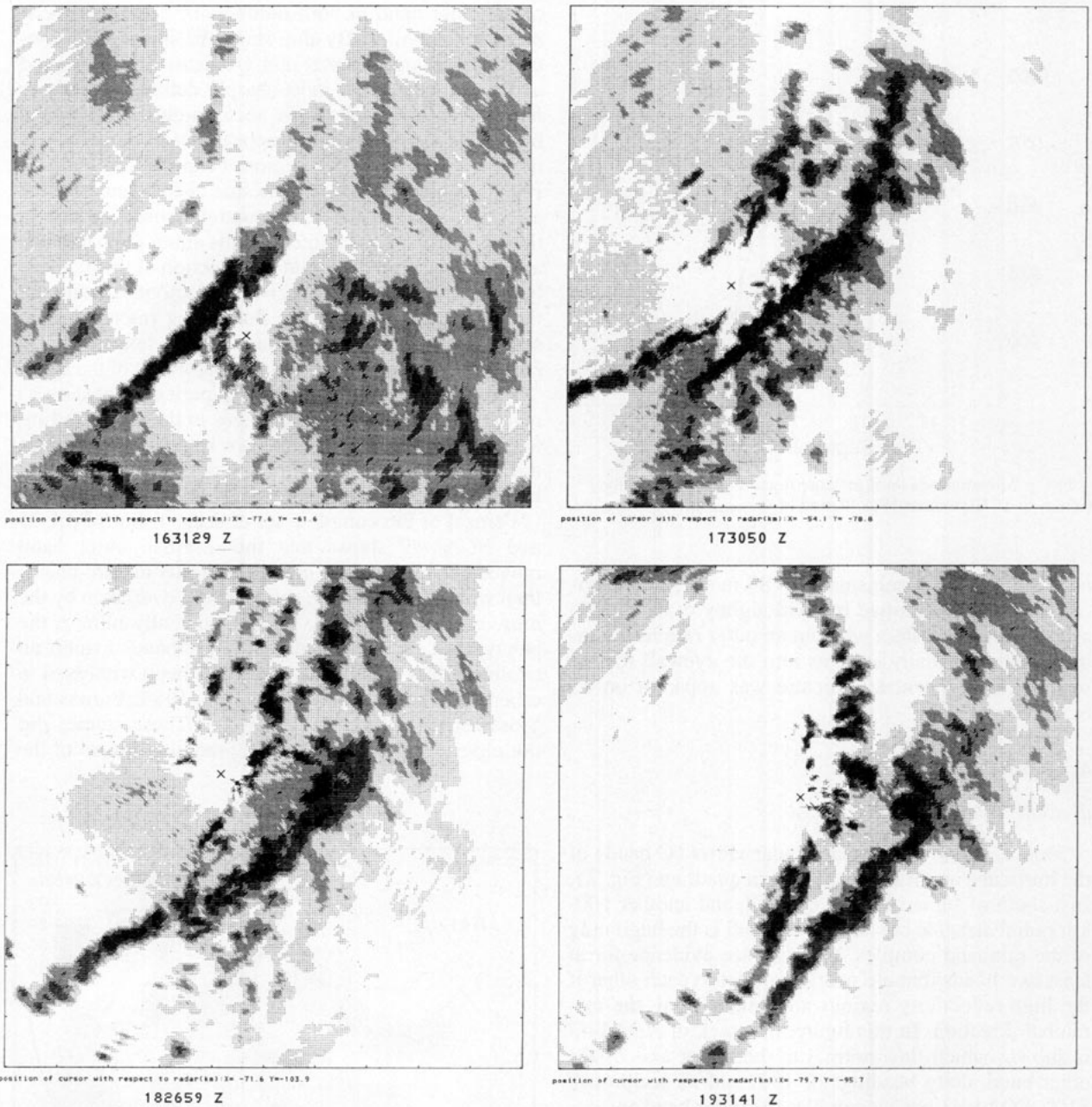
FIG. 3. An overview of rainband behavior during most of the experimental period from *NOAA-43*: (a) 1631, (b) 1730, (c) 1827, and (d) 1931 UTC. Increasing density of shadings start at 25 dBZ and increase in 5-dBZ increments. Each figure is 170 km × 176 km with north to the top. The aircraft position is marked by a cross.

older, mature band, nor were the reflectivities as strong as the Gilbert bands.

The typical reflectivity structure in the radius–height plane (Fig. 4) shows the extensive stratiform rain radially outward of the deepest convection that is part of the band major axis. This view is from *NOAA-42* as it flew nearly parallel to the major axis of the band. For the region outward from the convection there are radar returns greater than 22 dBZ to slightly

greater than 30 dBZ; the intensities vary from scan to scan through the experiment, but the region always appears to be under the influence of stratiform rain within 35 km of the band axis. Radially inward of the major axis there is little precipitation. The major axis contains reflectivities of 40 dBZ and the minimum detectable signal reaches a height of 14 km. Most of the stratiform portion of the band does not exceed 10 km in altitude.
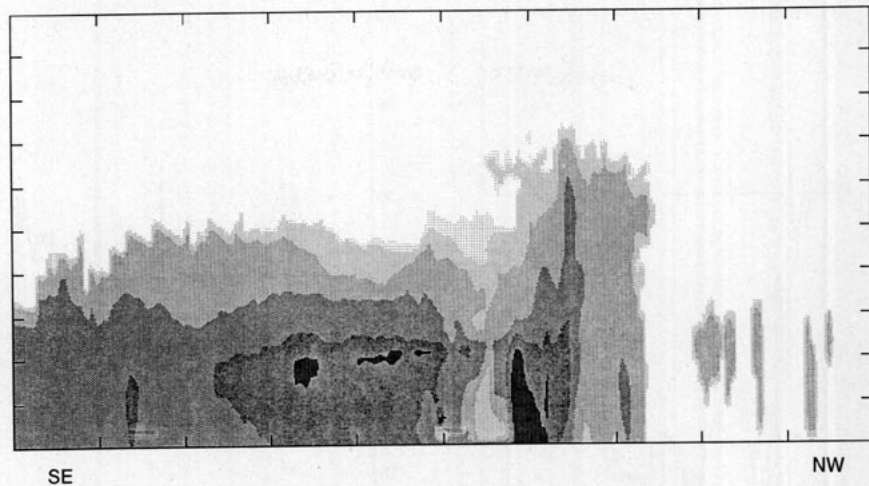
FIG. 4. Radius–height cross section of reflectivity from the tail radar of *NOAA-43* at 1705 UTC. Dimensions are 20 km (z) by 162 km (x) and the aircraft is at the 1500-m altitude and in the middle of the figure. Reflectivity shades are 5, 8, 15, 22, 30, and 37 dBZ.

b. A sample pass normal to the rainband

The passes normal to the rainband reveal strong and repeatable signals in both the wind and the thermodynamic variables. In Figs. 5a–f we present the relative radial and tangential flows, vertical velocity, D value, θ_e, and the temperature and dewpoint observed at the 720-m altitude for one pass normal to the band. The radial flow (Fig. 5a) is distinguished by potent inflow averaging -14 m s^{-1}, changing abruptly to zero inflow at 170-km radial distance. This steep gradient in V_R is indicative of horizontal convergence of -3×10^{-3} s^{-1}, assuming no divergence of V_T. Radially inward of this convergence zone there is nearly zero radial motion.

The V_T component (Fig. 5b) exhibits a somewhat noisy behavior for small horizontal scales in and near the band axis. There appears to be little systematic change in the band, but averaging several passes will reveal that V_T decreases in and near the high reflectivity. Examination of V_T for every pass in sequence does not provide evidence for divergence that would affect the magnitude of the convergence estimated from the change witnessed in V_R.

The vertical velocity signal for this pass (Fig. 5c), outward of the convergence zone located at 170 km, is dominated by mesoscale sinking averaging -0.4 m s^{-1}. A convective-scale updraft, collocated with the convergence zone, extends more than 6 km in the radial direction, achieves a maximum value in excess of 6.0 m s^{-1}, and is the primary feature apparent in Fig. 5c. This updraft is the channel of mixed-layer air that feeds the rainband. Downward motion appears radially inward of the primary updraft until the 140-km radius.

The D value (Fig. 5d) shows evidence for two scales of organization. The slope of the curve from the outer to the inner radii is due to the vortex-scale pressure gradient. Pressure decreases about 3.6 mb (36 m)

through the entire pass. Superimposed on the vortex-scale pressure field is a mesoscale pressure minimum from 195 to 166 km. This broad local minimum (see below the dashed line in Fig. 5d) is probably hydrostatically induced by the presence of the warmer, moister air found within both the active convection and the anvil that is radially outward of the band major axis. If the pressure minimum was caused by the interaction of the updraft with the shear, then we would expect the pressure minimum to be of similar horizontal scale of the updraft and about 90° out of phase with the updraft maximum (LeMone et al. 1988). In this pass the pressure minimum is nearly 30 km in horizontal extent. In the inflow portion (see Fig. 5a) pressure decreases approximately 3.0 mb.

An increase of θ_e with decreasing radius, which all the passes below 1 km have as a common characteristic, is shown in Fig. 5e. Note that θ_e increases 10 K in the 40 km adjacent to, but radially outward of, the convergence zone (210 to 170 km). The θ_e signal has a stair step quality despite aircraft altitude being nearly constant. It is possible that aircraft is flying through an undulating interface that separates two layers. In this case the larger values of θ_e are correlated with downward motion (see Fig. 5c). Inward of the convergence zone (160 km) θ_e decreases by several degrees in apparent response to convective-scale downdrafts.

The temperature and dewpoint are presented in Fig. 5f. The dewpoint is constrained to be equal to the radiometer measurement if it overshoots the dry-bulb estimate; this occurred only a few times during this pass (see near 170 km). Most of the passes below 1 km do not show evidence of saturation; even if one doubts the temperature readings at certain points along the track, there are reliable data for long segments at either end of the pass that verify the existence of the remarkable trend in θ_e. The generally unsaturated conditions support the visual observation that
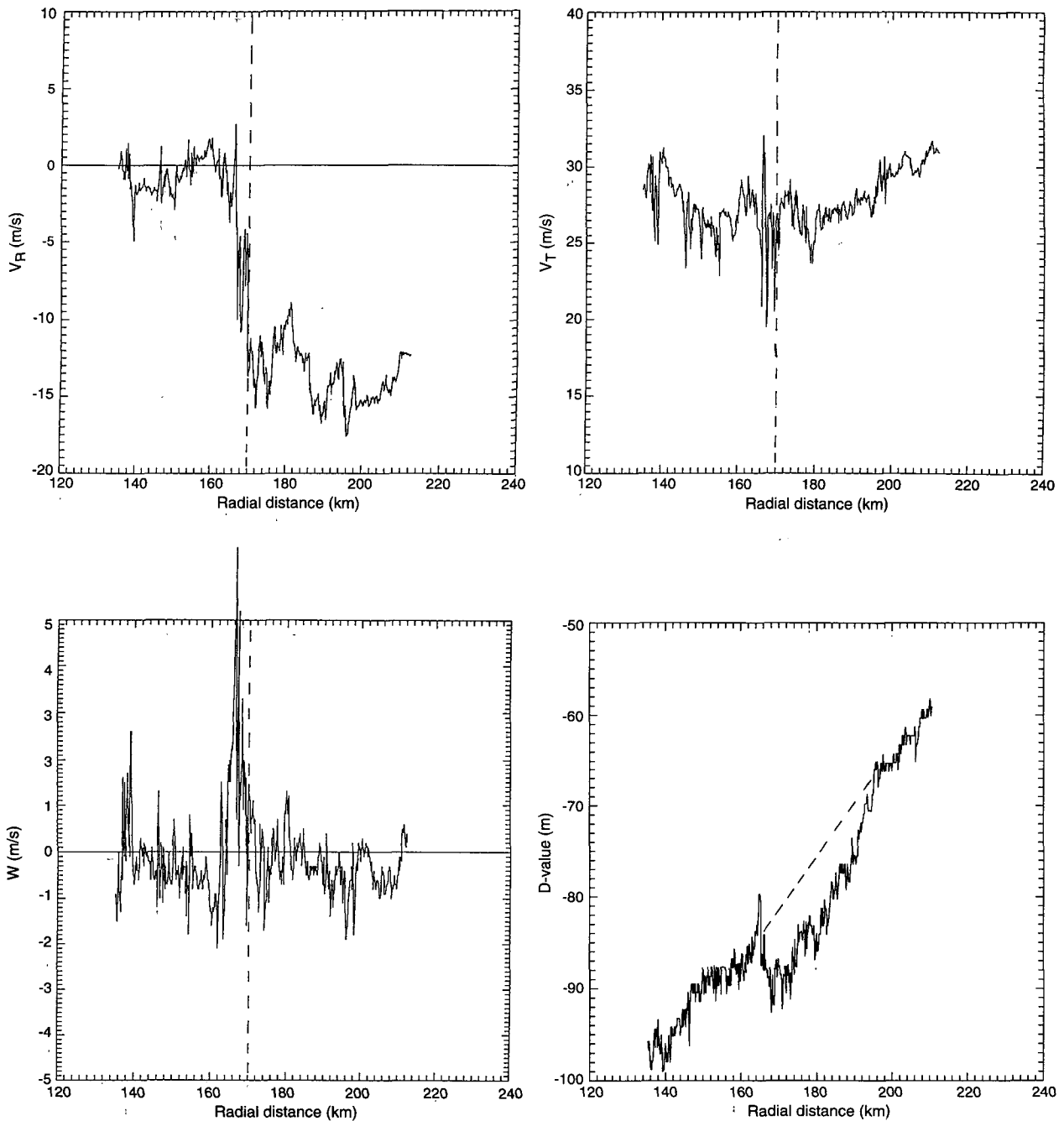
FIG. 5. A sample pass normal to the rainband from 1722:00 to 1731:10 UTC for *NOAA-43* at the 720-m altitude. Traces are (a) relative radial velocity V_R (m s^{-1}), (b) relative tangential velocity V_T (m s^{-1}), (c) vertical velocity W (m s^{-1}), (d) D,value (m), (e) θ_e (K), and (f) temperature and dewpoint (°C). The dotted vertical line delineates the outer edge of the convergence zone.

the aircraft is flying through light rain falling from a cloud layer that has a base higher than the aircraft most, but not all, of the time. Note that the temperature of the updraft (see Figs. 5c, 5f) is slightly cooler than the air found radially outward. The location with low θ_e ($\sim$160 km) is correlated with drier air, but not noticeably cooler air. There is apparently no cool outflow correlated with the

low-θ_e air found in the main convective downdraft at about 162 km.

c. Composite wind and thermodynamic fields normal to the band

The similarity of the signals in the aforementioned variables from pass to pass invites the creation of a
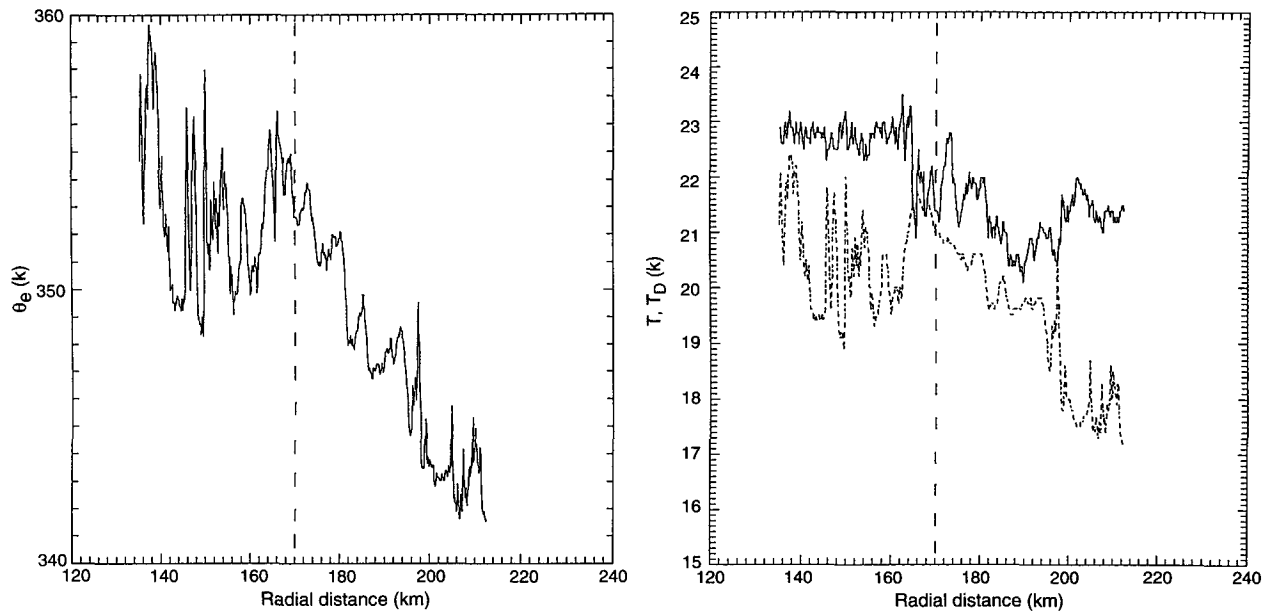
FIG. 5. (Continued)

composite over the 3-h flight experiment to develop a radius–height cross section centered on the rainband. The 19 passes flown normal to the band major axis are stratified into four levels of 300, 450, 700, and 1500 m. Data are placed relative to the sharp change of V_R found on the outer edge of the band major axis. Compositing with respect to the convergence rather than a certain radius preserves the gradients associated with the band and is not adversely affected by the band's changing location with respect to the storm center. The technique deemphasizes transient, convective-scale features. If there is more than one strong convergence zone, the composite is created with respect to the outermost convergence zone.

A sharp gradient in V_R denotes strong convergence if one assumes that the airflow changes parallel to the band are small. This assumption has been shown to be

reasonable for tropical cloud lines (Zipser et al. 1981), midlatitude squall lines (Wakimoto 1982), and hurricane rainbands (Barnes and Stossmeister 1986). The validity of this assumption for this particular band will be examined using wind fields derived from the Doppler radar of NOAA-42.

The radial wind component is shown in Fig. 6. The primary features are an increase in the inflow in the region radially outward of the convective cells, a sharp decrease to no inflow or slight outflow, and a region of weak, steady inflow radially inward of the convective cells. The increase in V_R outward of the convergence zone is strongest in the lowest 500 m and is weakest at 1.5 km. An average change below 1.5 km is from -8 to -15 m s^{-1} over 50 km; this would result in a vertical velocity of -0.15 m s^{-1} for this area under the anvil of the rainband assuming two dimensional divergence ($\partial V_R/\partial R + V_R/R = \partial W/\partial z$). Application of the same assumption to the convergence zone yields a mean up-
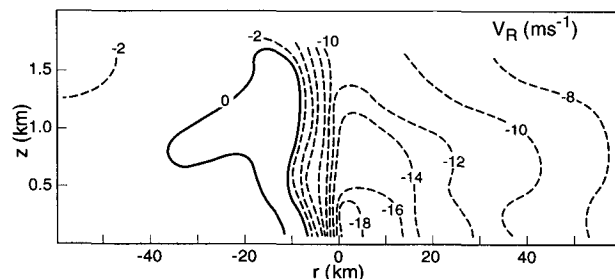

FIG. 6. A composite radius–height cross section of the relative radial wind component V_R (m s^{-1}) assembled from the 19 passes normal to the major axis of the band. The origin is at the outer edge of the convergence zone. Positive values of the radius are outward of the convergence zone.
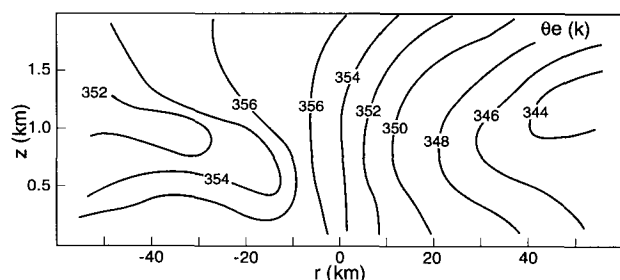

FIG. 7. As in Fig. 6, but for θ_e (K).
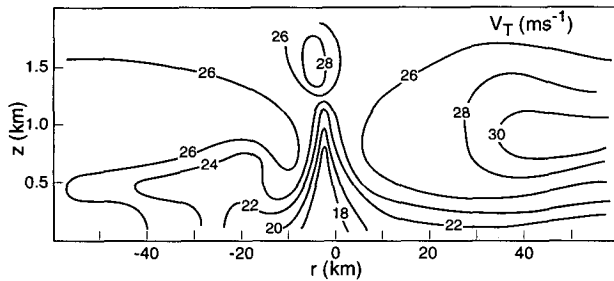
FIG. 8. As in Fig. 6, but for the relative
tangential velocity V_T (m s^{-1}).

draft in excess of 2.6 m s^{-1} at the 1.5-km altitude through the width of the convergence ($\sim$7 km).

The θ_e radial cross section in Fig. 7 shows an average increase of 7 K below the 1.5-km altitude in the inflow prior to reaching the convergence zone. At and just radially inward of this zone is where the mixed layer is tilted into the vertical to feed the rainband convective cells.

Radially inward of the convergence zone (-10 to -50 km), the θ_e field contains little or no horizontal gradient below 1.0 km. This region is more stratified in the vertical, in contrast to the relatively deep, well-mixed condition witnessed radially outward of the band. There is evidence of only a slight decrease in θ_e between -10 and -20 km (where the contours of θ_e curve downward). This is a reflection of the few transient convective-scale downdrafts that were sampled inward of the convergence zone. In Figs. 5c,e one can see a downdraft at 160 km that contains θ_e values that are several degrees less than the values in the main updraft or immediately outward of that feature.

In the V_T cross section (Fig. 8) the largest values are found 40 km radially outward from the band. A minimum in relative tangential flow exists at and below 1 km in the convergence zone; this was a consistent feature and not the result of averaging high and low values. At and above 1.5 km there is evidence of a maximum of V_T. The consistent nature of the minimum supports our belief that the divergence field is controlled by the behavior of V_R. If we witnessed small and large values of V_T from pass to pass, then it would have been possible for the tangential flow to either counteract or enhance the convergence inferred from the relative radial wind changes.

Perusal of the V_T and V_R fields in the lowest kilometers shows that the airflow changes its inflow angle from 35° 15 km outside the band to 0° or pure tangential flow 10 km inside of the edge of the convergence zone. Wind speed reduces about 4 m s^{-1} from $+40$ to -10 km in the subcloud layer as the flow becomes entirely rotational. Speeds near the surface increased slightly ($\sim$2 m s^{-1}) over the same distance. The air that is the source for the primary updraft of the rainband is clearly from the region radially outward of the band. Air be-

tween the rainband and the eyewall is continuing its approach toward the circulation center, albeit at a much lower radial velocity. If we were to examine the flow with respect to the rainband, which is moving outward at 3–4 m s^{-1}, all the flow would be inward and the small region of $+V_R$ would disappear.

d. Apparent rapid increase of energy in the inflow

Figure 9 contains three vertical profiles of θ_e, assembled from the radius–height cross section shown in Fig. 7. During the time it takes for the air to move the last 35 km to the convergence zone, there is a mean increase of 7 K over the lowest 1500 m. From the convergence zone to 35 km farther inward θ_e is nearly constant when the entire layer is considered, in stark contrast to the outer 35 km. The increase of 7 K is approximately equivalent to 7000 J kg^{-1} of moist static energy ($C_p\theta_e = h$); for the 1500-m-deep column with an average density of 1 kg m^{-3} an increase of 1.05×10^7 J is required. A mean inflow rate derived from Fig. 6 is -12 m s^{-1}, therefore the column has slightly less than 3000 seconds to receive the energy before it reaches the convergence zone and the convective cells of the rainband. *If all this energy were to come from the sea surface, then a combined heat and moisture flux exceeding 3500 W m^{-2} is required to balance the budget.* This is substantially more than the combined heat and moisture flux for undisturbed conditions in the equatorial trough (e.g., $\sim$100 W m^{-2}, Barnes et al. 1980) and two times greater than the largest values at the sea surface estimated by Betts and Simpson (1987) for an inflow region based on the observations in the inner core of Hurricane Daisy (1958). The surprise is not just the mag-
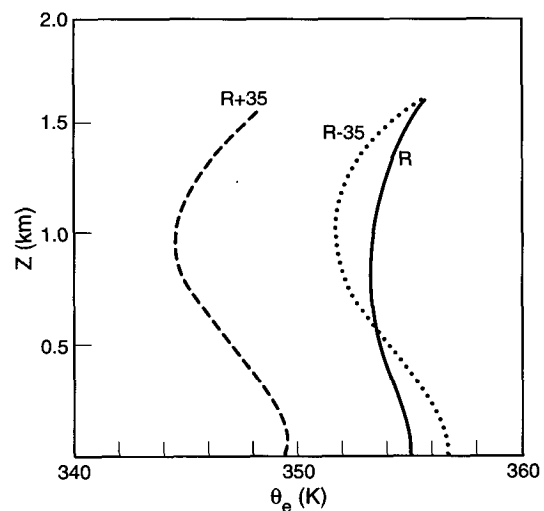

FIG. 9. Profiles of θ_e (K) for the lowest 1.5 km, taken from the composite, Fig. 8, for three locations: 35-km radial outward of the band (solid), the outer edge of the convergence zone ($r = 0$, dashed), and 35-km radial inward of the convergence zone (dotted).
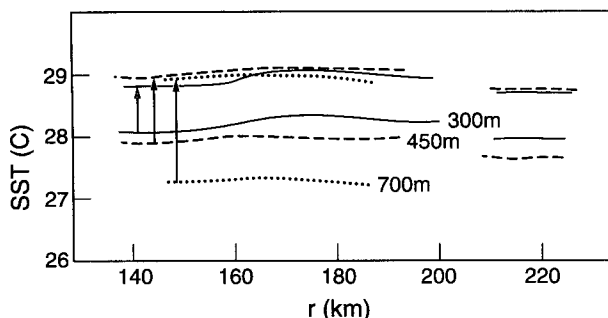
FIG. 10. Raw and corrected radiometer SSTs from *NOAA-43* for three altitudes (300, 450, and 700 m) as a function of radial distance for the region near the rainband.

nitude of the required fluxes, but their location. Usually the rapid increase of θ_e is seen adjacent to the eyewall (e.g., Hawkins and Imbembo 1976; Jorgensen 1984), not 170 km radially outward from the storm center. Wind speeds adjacent to the rainband are not increasing rapidly like they are near an eyewall. In the final 35 km prior to the convergence zone, wind speed near the surface increases from 21 to 23 m s^{-1} (see Figs. 6 and 8). Arguments that invoke a transfer coefficient–wind speed relationship might be used to explain the increased fluxes near the eyewall, but not for the region adjacent to the Gilbert rainband. We apparently have a deep layer of inflow that is undergoing a remarkably rapid increase in θ_e or moist static energy.

e. Estimated surface sensible and latent heat fluxes

Our ability to measure the energy exchanges at the interface is challenged by sea-spray evaporation, sensor wetting, and the uncertainty of the transfer coefficients (Powell 1990b). Ship observations close to the eyewall are currently impractical. Compounding the measurement issue is the likely high spatial variability of the fluxes given the significant overturning of the oceanic mixed layer by the tropical cyclone and subsequent lowering of sea surface temperature (SST, e.g., Black 1983; Shay et al. 1988).

To obtain an estimate of the fluxes we invoke the bulk aerodynamic equations; to apply these equations we need to know the gradients of temperature and moisture between air and ocean, the wind speed at 10 m, and the transfer coefficients. We shall purposely estimate the sea surface fluxes generously to demonstrate that the surface fluxes alone cannot account for the observed increase of θ_e in the inflow layer.

NOAA-43 is equipped with a downward-looking radiometer that can provide an estimate of SST. Unfortunately, the radiometer receives radiation not only from the sea but also from the water vapor in the intervening layer. We make a simple correction based on the change in the sensed SST as a function of aircraft altitude; implicitly we are assuming that the intervening

layer is well mixed. The scheme is not applicable in the presence of clouds or heavy rain. A more complex correction, based on buoy and expendable bathythermograph data, has been used by Black (1993, personal communication). The correction that we use here obtains a similar result, but our scheme is really at its best for low altitudes ($z < 500$ m). The raw and corrected SSTs appear in Fig. 10. We do not attempt to correct the raw SST values when the aircraft is in heavy rain or cloud, hence the gaps in the sample traces. The passes made at 300–700-m altitude all estimate an SST slightly above 29°C when the linear correction is made for the depth of the intervening layer. Though 700 m is above the mixed layer, the amount of air with very different water vapor content is so small that the "corrected" SST differs from the other, lower levels only slightly. Maximum SST is not more than 29.2°C using this method, and it is a straightforward process to estimate the saturated specific humidity of the thin surface layer (26 g kg^{-1}) that is assumed to exist in the bulk aerodynamic formulation.

To estimate the temperature T and specific humidity q at 10 m we first assume that the 300-m altitude passes made by *NOAA-43* were in the mixed layer. Soundings made outward of the band show a nearly dry adiabatic and well-mixed layer through the lowest 300–400 m. A composite sounding from *NOAA-42* (Fig. 11, that will be discussed in more detail in section 5) shows the T and the dewpoint temperature T_D in the region radially outward of the band that supports our contention that the layer is mixed and dry adiabatic below 300 m. Based on these assumptions we obtain $T \approx 27$°C and $q \approx 18.0$ g kg^{-1} as mean values at 10 m. To estimate the wind speed at 10 m we follow the empirical findings of Powell (1987), who compared flight level wind speeds to surface speeds from buoys. Powell (1987) found that the surface wind is in the range 0.7–0.9 of
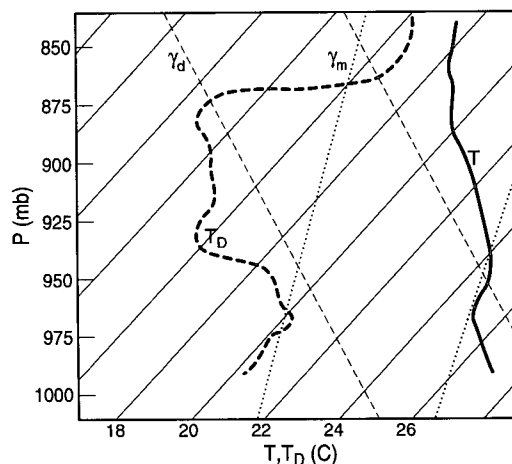

FIG. 11. Temperature (solid) and dewpoint temperature (dashed) on a skew T–log$p$ diagram for a composite sounding representative of conditions found radially outward of the rainband.

the wind speed at 500 m. We have assumed a coefficient of correction of 0.9, which yields a mean wind speed of 21 m s^{-1} for the inflow region.

Finally, we must estimate the transfer coefficients. Large and Pond (1982) estimated the drag coefficient for a wide range of observations and argue that above 10 m s^{-1} the drag coefficient slowly increases, but the certainty of this relationship is plagued by a lack of data above 25 m s^{-1}. Refinements to their findings await improved instrumentation applied to high wind situations. The transfer coefficients for sensible (C_H) and latent (C_Q) are a function of the drag coefficient (C_D) and are estimated to be 1.6×10^{-3} and 1.7×10^{-3}, respectively. With all of the necessary variables and coefficients, some of which we have chosen liberally to estimate the highest fluxes possible, we find the sensible heat flux to be 90–110 W m^{-2} and the latent fluxes to be 800–1000 W m^{-2}. This calculation shows that fluxes from the sea can supply less than one-third of the energy necessary to explain the observed increase in the inflow. The crucial measurement that affects the estimate of the needed fluxes is the depth of the layer that undergoes an increase of θ_e, which is at least 1.5 km thick.

To understand the evolution of the inflow we need to consider the fluxes at the top as well as at the base of the inflow layer. Also, we have assumed that the air follows a simple pathway to the rainband based on the two-dimensional cross sections. Therefore, we shall 1) analyze the three-dimensional wind fields from the Doppler data to verify the accuracy of the airflow assumed from the cross sections, and 2) use this wind field and the observed thermodynamic fields to initialize a general structure entrainment model like that used by Powell (1990b) to estimate the fluxes at the top of the inflow layer as well as those at the sea surface. Results from the simulation will be presented in section 5.

f. Doppler-derived wind fields

Figure 12 is a depiction of the rainband, the stratiform region found immediately outward of the convective cells and the "L" pattern completed by NOAA-42. The "L" takes 12 minutes to finish, which prevents analysis of convective cells that likely complete a significant portion of their life cycle during this period. For this particular volume we have several reflectivity maxima that move at varying velocities. This means that the identification and application of any one advection velocity, which corrects for the movement of the air during the sampling time, will smear the wind field for other reflectivity features that may be moving at different velocities. We have averaged the u and v components for several reflectivity maxima, realizing that this may produce questionable wind fields for the stronger cells in the volume. Because of this and the time it takes to complete the volume scan, we have
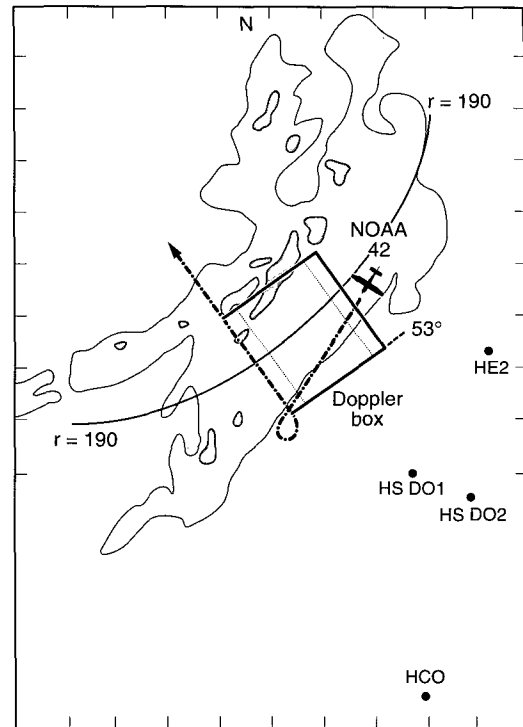

FIG. 12. Track of NOAA-42 (chain dashed line with arrows) and region analyzed with the Doppler radar (bold square), on the reflectivity field as seen with the lower fuselage radar from NOAA-43 (see Fig. 2). Reflectivities greater than 25 and 35 dBZ are shown. Locations of the four soundings (HE1, HE2, HSDO1, HCO) made by NOAA-42 are shown. The dotted lines show the locations of the x–z Doppler cross sections. The entire radar depiction is 180 km × 252 km.

elected a conservative approach whereby we remove scales of motion smaller than 5 km through the use of a low-pass filter. We shall concentrate on the identification of the mesoscale horizontal flow fields radially outward of the convective cells, not the vertical velocity fields associated with the cells themselves.

The Doppler data can be used to verify the cross section of the radial flow component (see Fig. 6) that shows that the air undergoing the rapid energy increase is flowing toward the rainband from the southeast or larger radii. Figures 13a,b are two vertical slices of V_R through the target volume (see the location of these two slices in Fig. 12) that are parallel to the aircraft in situ cross section. These slices have strong inflow below 2 km with the inflow depth decreasing as it approaches the band. The radar cannot see the lowest 500-m altitude very well due to sea clutter effects, nonetheless the inflow of -12 to -15 m s^{-1} is comparable to the winds from the aircraft inertial navigation system (INS). Note that there is strong shear with the inflow reversing to outflow by about 2 km. By the 3.5-km altitude the outflow, which is relative to the circulation center, is in excess of 3 m s^{-1}. The mean vertical shear
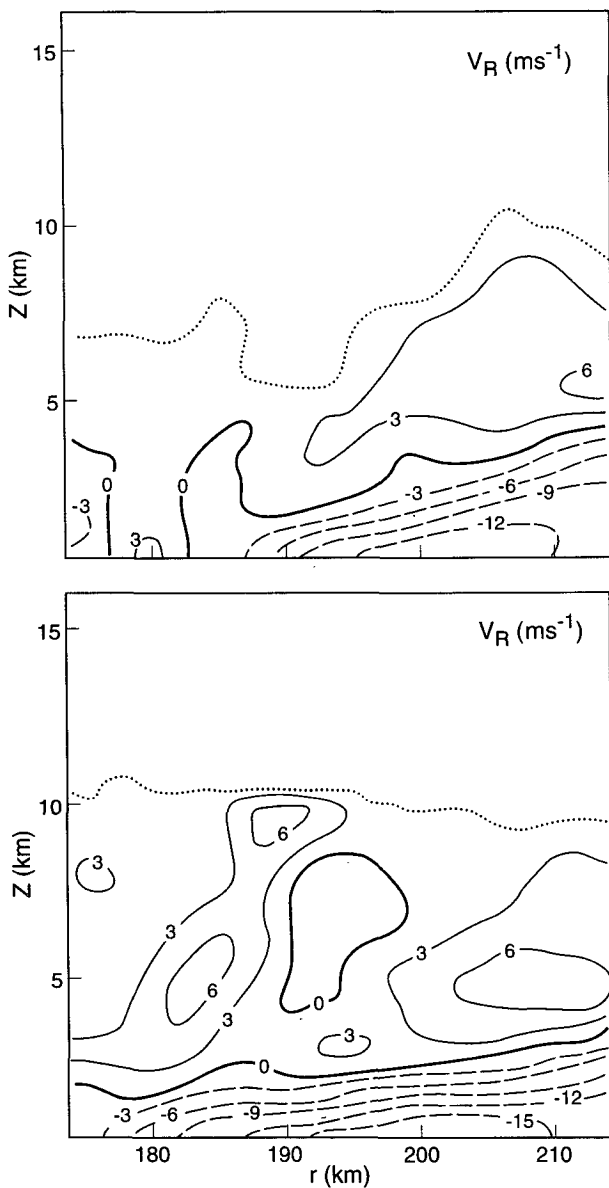
FIG. 13. (a) Radius–height cross section of V_R 30 km northeast from the southwest edge of the Doppler box. Dashed contours are inflow $(-V_R)$, solid contours are outflow $(+V_R)$. Contour interval is 3 m s^{-1}. The fine dotted line shows the maximum height where minimum detectable signal was last sampled. (b) Same as (a) but for 6 km from the southwest edge of the Doppler box.

also show the limits of return in the vertical, which is only about 10 km for most of the slice. This is several kilometers shallower than the tallest cells found along the major axis of the band (see Fig. 4). The deep radial outflow and the low level of the minimum detectable signal support the contention that this band is not detraining air in a thin layer near the tropopause. Low cloud tops and a thick layer of detrainment are indirect evidence for relatively modest CAPE present in the inflow to the band. We shall explore the issue of CAPE in section 4g.

Radius–height cross sections for the tangential wind component are presented in Figs. 14a,b. The V_T slices
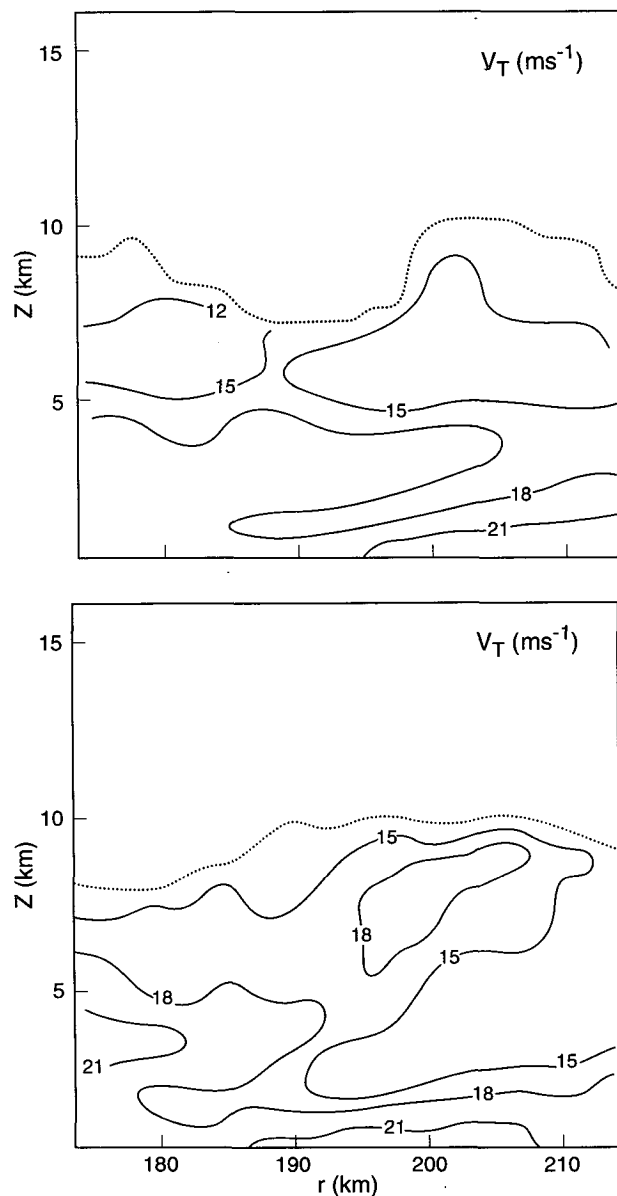
FIG. 14. (a), (b) Same as Fig. 13 but for V_T. Positive flow is cyclonic and into the page.

of the radial wind component through the lowest 3 km exceeds -6.0×10^{-3} s^{-1}. In section 4g the ramifications of such strong shear for the rainband circulation will be discussed. The Doppler analysis spreads the convergence zone over about twice the distance (15 versus 7 km) that the in situ sensors record. The filtering necessary due to the long sampling time and evolution of the field are the primary causes for this aliasing of the convective-scale convergence. Figures 13a,b

are also homogeneous throughout the target volume with the strongest cyclonic flow in the lowest levels, as would be expected for a warm-core system. The Doppler cannot resolve the strong shear in the lowest 500 m, nor can it resolve variations on horizontal scales less than 5 km. However, the mesoscale aspects of the flow radially outward of the band match the in situ analysis to within 2 m s^{-1}.

Figures 15a,b are horizontal ($x-y$) slices for the V_R and V_T components at the 500-m altitude. A high-reflectivity region or cell along the rainband axis near 180, -10 corresponds to the $+V_R$ flow in Fig. 15a. In Fig. 15b the minimum in the rainband ($X = 180-185$ km) is close to the value that the aircraft INS samples. The Doppler region does not extend outward as far as the in situ winds so we do not see the strong divergence signal clearly.

The wind fields from both the Doppler and the in situ sensors suggest that the inflow is approximately 2.0 km deep. If the rainband could be adequately described as a simple two-dimensional circulation in the radial direction, an outflow 7–8 km thick would be required to balance the observed inflow. The Doppler-derived winds show that this appears to be happening, with an outflow rate of 4 m s^{-1}. The rainband circulation is one of low-level radial inflow and mid- to upper-level radial outflow. The difference between this band and an eyewall is that the outflow is not confined to the upper troposphere; it has substantial outward mass flux by the 2–3-km height.

The flow is homogeneous over a 30 km × 30 km region adjacent to the band. There is no evidence to suggest that the lower-θ_e air that is farther from the band follows a different course from that suggested by the two-dimensional in situ analyses. This means that this air will serve as inflow to the band. A second look at Fig. 3 shows that the high-reflectivity portion of the band extends well to the northeast of the Doppler analysis region. To maintain an equivalent intensity farther to the northeast, it is probable that the instability along the outer edge of the band is approximately equal all along the outer edge. If the instability is similar all along the outer edge, then it follows that the low-θ_e air on the outer edge of the Doppler analysis must be increased to a value close to what was witnessed near the band. Another way to increase the instability would be to cool the air in the mid- and upper troposphere, but there is no evidence of this based on the ferry legs (430, 550, and 700 mb) to and from the hurricane.

g. Environmental conditions

A deep sounding (HE2, shown in Fig. 16) taken by *NOAA-42* about 70 km east-southeast of the rainband (see Fig. 12) provides an estimate of the environment. If a representative parcel from the mixed layer is lifted, it will condense near 890 mb but will not become buoyant (level of free convection—LFC) until 775 mb. The
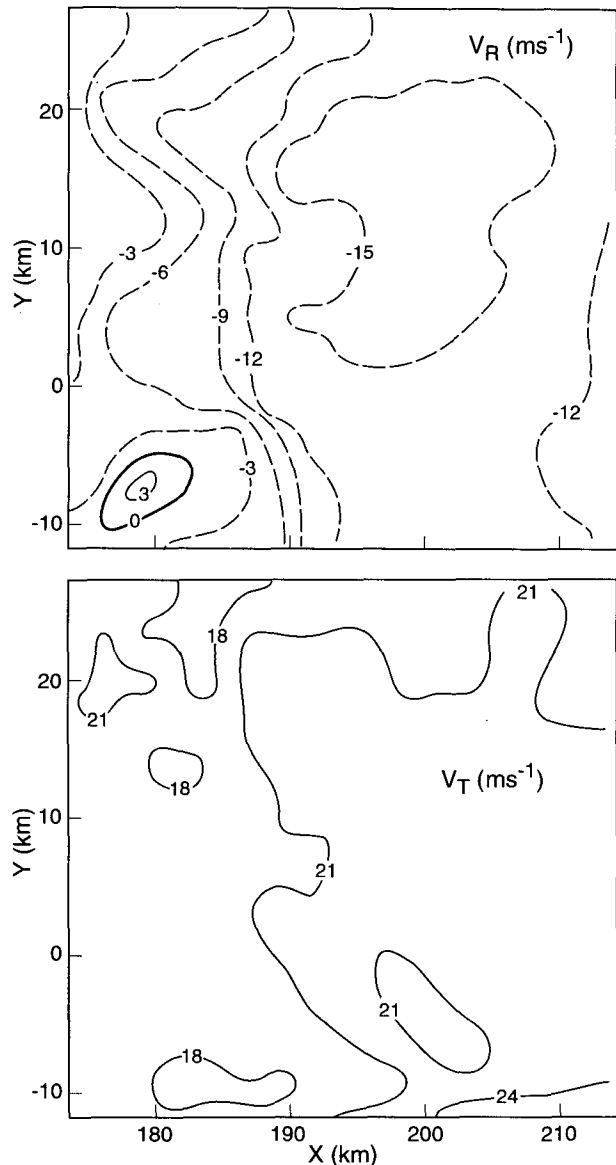

FIG. 15. Horizontal slices at 500 m for the Doppler region for the (a) V_R component and (b) V_T component.

considerable convective inhibition (negative area, 37 m^2 s^{-2}) must be overcome by forces other than buoyancy. The convective available potential energy (CAPE), which can only be measured to maximum aircraft altitude (430 mb), is approximately 140 m^2 s^{-2}, and the lifted index is only $-1.4°C$. This marginal instability is for air that has not yet undergone the large increases of moisture that were diagnosed for the subcloud-layer inflow. The passes normal to the band show that the pseudoadiabatic path of the parcel may increase by as much as 2 K. If we assume no warming aloft, then CAPE is more likely near 450–500 m^2 s^{-2} from the LFC to 430 mb. This value is close to the
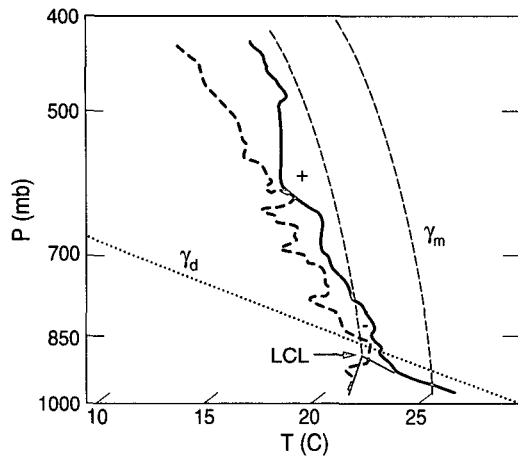
FIG. 16. A skew T-log$p$ diagram showing temperature (solid) and dewpoint (dashed) for sounding HE2 completed by *NOAA-42*.

instability observed for this portion of the atmosphere for other bands (e.g., Hurricane Raymond, Barnes et al. 1991). Of course the environment modulated by the presence of a hurricane vortex may not need much instability to produce strong vertical motions. McCaul (1991) shows that when hurricanes make landfall they can yield tornadic cumulonimbi in an environment with very little CAPE.

The most vital specification for the simulations is the initial sounding to determine the mean conditions of the inflow and the lapse rates above this layer. Aircraft passes normal to the band were not made above 1500 m so we use soundings and Omega dropwindsondes (ODWs) obtained on the outer side of the band by *NOAA-42*. The locations of the four aircraft soundings are shown in Fig. 12. The original desire was to obtain a view of the environmental structure, not the internal portions of the band, so these soundings range from 50 to 100 km from the band major axis. We do not have soundings available for the Doppler analysis region (see Fig. 12), which is where the simulation begins.

All of the *NOAA-42* soundings outside of the band show a structure that is unlike typical, tropical conditions (e.g., Jordan 1958; Barnes and Sieckman 1984). An analysis of conserved variables will highlight the important, repeatable structures found outward of the band. Conserved variable diagrams in the form of q–θ_e plots (Paluch 1979) have been used to study the mixing processes of the convective boundary layer in the Tropics (Betts and Albrecht 1987) and the origin of the boundary layer in the vicinity of an oceanic front (Rodgers 1989). While total water is the usual choice on diagrams such as those employed by Paluch (1979), we use q since the majority of the soundings were completed in regions of stratiform cloud where the liquid water contribution is small.

We plot data from the two deep environmental soundings (HE1, HE2) made to the northeast of the

rainband and two shallow soundings (HCO, HSDO1) made under the anvil cloud nearer the band in Fig. 17 to illustrate the variability in the thermodynamic structure found on the outer side of the rainband. These data show a lower-mixing-line structure characteristic of vertical mixing between the surface layer (top at about 980 mb) and the top of the convective boundary layer (about 920 mb for the deep soundings, about 870 mb for HCO). Extrapolation of the lower mixing line would intersect the surface at a θ_e value near 360 K indicative of surface layer air modified by a sea surface temperature of 29°C. Unusual features in Fig. 17 are the prominent kink in the sounding for HCO at 870 mb and a less distinct kink for HE1 and HE2 (the deep environmental soundings) at 920 mb. In addition to HCO, the HSDO2 outer sounding (not shown) also displayed a prominent "q reversal." A q reversal has been described by Betts and Albrecht (1987) in terms of evaporation and precipitation processes. The minima in the q–θ_e curve at 870 and 920 mb represent air transported down from above via an evaporation-driven penetrative downdraft or a mesoscale downdraft beneath the stratiform rain on the outer side of the rainband. There is a sharp increase of q at the top of the inversion that serves as the base of an upper-mixing-line structure. Evaporation of shallow clouds mixing with a drier subsidence layer could act to shift the mixing line vertically, creating the upper line between 870 and 830 mb on the deep environmental soundings. An extension of this line appears in the upper part of the HCO sounding. Alternatively, a q reversal could also be caused by differential advection between the relatively dry inflow beneath the rainband anvil and the
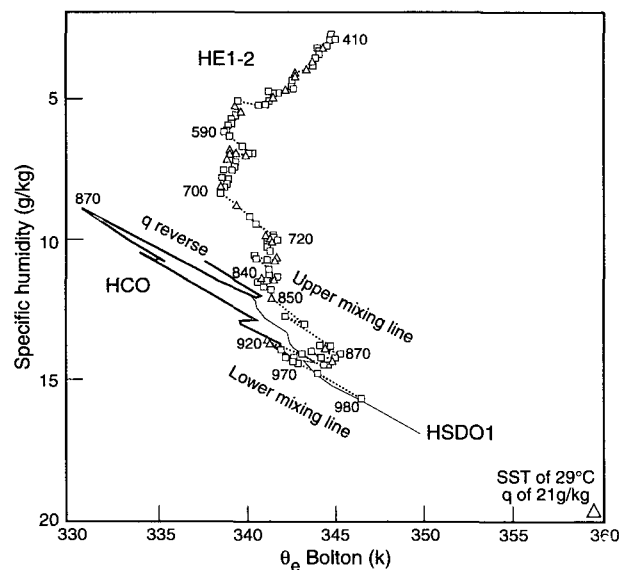

FIG. 17. The q–θ_e plots that include data from the two deep environmental soundings (HE1, HE2) and two shallow soundings (HCO, HSDO1) under the anvil of the rainband.

overlying moist outflow originating from the convection near the band axis. Strong shear in the vicinity of this moisture source may enhance turbulent mixing across the interface between outflow and inflow, increasing θ_e in the inflow as the air moves closer to the rainband axis.

Additional information was sought from the several ODW drops during the experiment. Unfortunately, an ODW yields inaccurate humidity values if the sonde passes through clouds or rain, but it does provide reasonable temperatures. The ODWs confirm the T structure obtained from the aircraft sensors.

We have combined several of the stair-stepped and regular soundings completed by *NOAA-42* to create a "best guess" of the thermodynamic structure found outward of the band (Fig. 11). The composite structure includes a mixed layer below about 945 mb, a dry layer from this level to about 890 mb, and finally a moister layer with a moist adiabatic lapse rate above 870 mb. We suspect that the layer above 870 mb would become saturated if we had the good fortune to observe the thermodynamic structure within the Doppler analysis region.

The other aspect to the environment is the wind field. We do have wind data for the region adjacent to the band from the Doppler analysis. A hodograph derived for the region radially outward of the convergence zone (Fig. 18) shows strong inflow below 1 km, changing to nearly tangential flow above 2.0 km. Above this level air is still strongly cyclonic but heading outward with respect to the circulation center. Shear through the first 3 km exceeds 6.0×10^{-3} s^{-1} and is primarily found in the radial wind component. The role that this high shear and modest CAPE have in the formation of the return flow will be discussed in the next section.

h. Return flow as a function of environmental conditions

Thorpe et al. (1982) and Rotunno et al. (1988) have argued that a balance between the shear generated in the cold outflow and the environmental shear will produce updrafts that are more erect in the lower troposphere and thus favor deeper convection. This balance can be stated as

$$(\Delta u)^2 = 2 \int g \frac{\Delta \theta}{\theta} \, dz \equiv C^2 ,$$

with $\Delta \theta$ the mean cooling over the depth of the outflow and Δu the environmental shear usually measured over the depth of the cold dome. If the shear extends through a depth that is much greater than the cold dome, then Weisman et al. (1988) suggest that C should exceed Δu by a factor of 2, otherwise the environmental shear will tilt the updraft quickly downshear and limit the height of the convective cells. We have used the passes through the band to estimate the depth and magnitude of the cold outflow for the band. We find that the cold
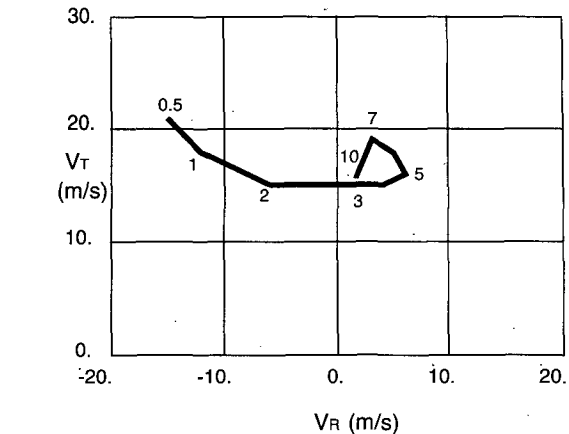

Fig. 18. A hodograph from the Doppler winds for a target volume representative of the region radially outward of the band in V_R–V_T coordinates. Units are meters per second.

dome is remarkably small and weak, averaging a horizontal extent of only 4 km, a vertical extent of 750–1000 m, and an average $\Delta \theta$ of −0.6 K. One of the largest T decreases can be seen in Fig. 5f where there is a mean decrease in T of about 1°C at 170 km. This is in contrast to most tropical MCSs that have a cold dome of air that covers many tens of kilometers in the direction normal to the convective cells along the leading edge (Barnes and Garstang 1982). We estimate $C^2 \sim 30$–40 m^2 s^{-2}. The square of the shear through the depth of the cold dome $(\Delta u)^2$ is about 64 m^2 s^{-2} and through the lowest 3 km is 324 m^2 s^{-2} (see Fig. 18). The vorticity in the environmental flow is stronger by a factor of 2 over the depth of the cold dome and is nearly an order of magnitude larger when one considers the lower troposphere. The shallow, only slightly cool outflow is dominated by the environmental shear, creating a situation favoring a shallow return flow. The low CAPE will not be able to rectify this sloped condition. Updrafts of 4 m s^{-1}, a typical value observed with the Doppler radar along the major band axis, combined with outflow of a similar strength will produce an outward tilted updraft column with a mean slope of 45°.

5. Results—Simulation

a. Numerical simulation background

The energy flux into the mixed layer has been the subject of numerous efforts starting with the zero-order jump models of Ball (1960) and Lilly (1968). This type of model, which reduces the transition layer to a first-order discontinuity, has been applied to the recovery of tropical squall-line wakes with a reasonable match to observed conditions (e.g., Fitzjarrald and Garstang 1981; Nicholls and Johnson 1984). Nicholls and Johnson (1984) have also employed the General Struc-

ture Entrainment Model (GSEM) developed by Dear-
dorff (1979) with similar success. Powell (1990b) has
used the GSEM to determine the recovery rate of
downdraft air as it departs from a convectively active
rainband and flows toward the eyewall. The application
of the models to either squall wakes or hurricane rain-
bands has demonstrated that

1) lapse rates of q and S_v (virtual dry static energy)
above the mixed layer have a major effect on the fluxes
at the top of the layer,

2) subsidence or mesoscale sinking inhibits the
growth of the depth of the mixed layer, but it does not
alter the thermodynamics within the mixed layer,

3) the entrainment of dry air found in the subsiding
air above the mixed layer can produce a further reduc-
tion in θ_e of the mixed layer and delays the replenish-
ment to typical environmental conditions,

4) rainfall evaporation cools an unsaturated mixed
layer, but it has no effect on the θ_e of that layer,

5) rainfall can effect the entrainment rate at the top
of the mixed layer via differential evaporation and sub-
sequent differential cooling between the transition and
mixed layer, and

6) divergence controls the rate of subsidence that,
in turn, affects the gradients of moisture and S_v at the
top of the mixed layer, the rate of growth of the mixed
layer, and thus what kind of air gets entrained into the
mixed layer.

To simulate mixed-layer characteristics of the inflow
to Gilbert's rainband, we used the GSEM developed by
Deardorff (1979) but modified with the moisture flux
parameterization for the top of the mixed layer that was
used by Nicholls and Johnson (1984). The GSEM
avoids the typical closure assumption of the earlier
models that parameterized S_v flux at the top of the
mixed layer in terms of the surface flux. In the GSEM,
S_v flux is assumed to be zero at the top of the mixed
layer and at maximum within the transition layer
(Deardorff 1979). The GSEM contains a detailed ex-
pression for entrainment velocity (w_e, see Nicholls and
Johnson 1984), which helps to control the thickness of
the mixed layer, the moisture flux at the top of the
mixed layer, and the jumps of S_v and q above the mixed
layer. Unfortunately, due to a dependence on surface
S_v flux, the GSEM formulation of q flux at the top of
the mixed layer does not allow downgradient flux when
a positive jump of q exists at the top of the mixed layer.
This discrepancy is solved by substituting the expres-
sion for q flux contained in Nicholls and Johnson's
(1984) model. Hence, the flux of q is a function of the
entrainment rate at the top of the mixed layer, the gra-
dient of q found at the interface, and evaporation dif-
ferences between the mixed and transition layers. The
in situ data show that there is strong shear across the
top of the inflow. We have included a parameterization
of the enhancement of entrainment due to wind shear
between the top of the mixed layer and the transition

layer as described by Fairall (1984). A wind shear of
6 m s^{-1} is prescribed over the transition layer. This
shear produces a flux Richardson number in excess of
the critical value of 0.5, resulting in a 20%–80% en-
hancement of entrainment along the trajectory, com-
pared to runs with a standard GSEM w_e approximation.

b. Initial conditions for the simulations

We must specify the fields of velocity, subsidence,
fluxes of heat and moisture at the sea surface, the lapse
rates of S_v and q in and above the transition layer, and
the rain rates along the trajectory. The velocity field is
a function of the wind fields derived from the Doppler
with subsidence specified from the in situ divergence
estimates. Fluxes of heat and moisture from the sea are
calculated using the bulk aerodynamic equations. Rain
rates are determined from the observed reflectivity pat-
terns and a $Z–R$ relationship for hurricanes (Jorgensen
and Willis 1982). The initial conditions for the simu-
lation are based on two sources of information. The
conditions below 800 m are derived from the passes
normal to the band and about 35 km from the major
axis of the band (see Fig. 9, +35-km profile). We have
smoothed the structure below 800 m to produce a well-
mixed layer. This results in a mean $\theta_e = 345.5$ K for
the mixed layer. Above 800 m we have used a positive
lapse rate of θ_e based on the composite sounding (Fig.
19). Above 870 mb θ_e increases with height around 10 K.
This increase in θ_e actually may be conservative in that
the layer directly above the inflow is not saturated in
the composite sounding, but it probably is within 30–
40 km from the band.

c. Simulation results

The column of air travels 90 km (equivalent to 35-
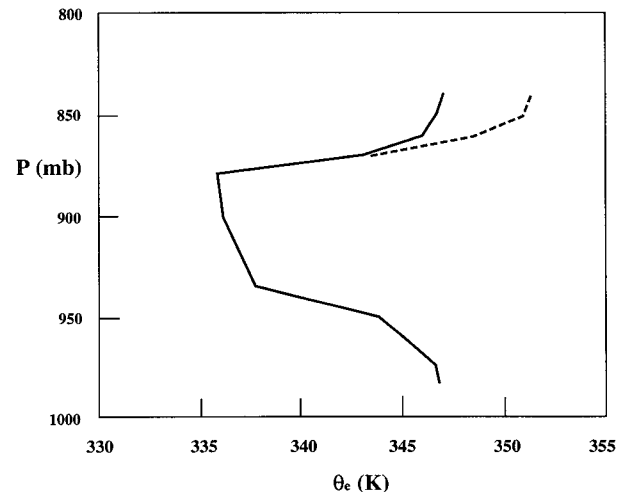km radial distance) before it reaches the outer edge of

FIG. 19. Equivalent potential temperature for the composite sound-
ing shown in Fig. 11 (solid) and if the layer above the inflow is
assumed to be saturated (dashed).

the convergence zone diagnosed with the cross sections. Table 1 contains a summary of the initial conditions and a subset of the simulations that were run. All these runs have a positive jump of q and S_v at the top of the mixed layer. Simulations without the positive jump in moisture at the top of the mixed layer do not lead to large increases of θ_e like these runs do. In Table 1 the five runs vary in what processes are included. Run 58 has no rain, no subsidence, and no shear at the top of the mixed layer. The other runs include only one of these processes except for run 65, which contains the complete set of processes. Note that the inclusion of rain (run 56) deepens the mixed layer but increases the mean θ_e only slightly when compared to run 58. Subsidence (run 55) suppresses development dramatically with the mixed layer thinning to 682 m from its original 800 m. Enhanced entrainment due to shear across the transition layer (run 64) deepens and moistens the mixed layer. The results of the simulation with all these processes (run 65) is presented schematically in Fig. 20. Surface sensible and latent heat fluxes vary from 214 to 164 W m^{-2} and from 1535 to 997 W m^{-2}, respectively, along the trajectory. Latent heat flux at the top varies from 3000 to 540 W m^{-2}. The flux at the top decreases as both the entrainment velocity (see Fig. 20) and the gradient of q across the top of the mixed layer weaken. Changes in S_v are small because rain evaporates in the mixed layer.

Run 65 does produce a large increase in the mixed layer, but the total amount of energy that is placed into the mixed layer is only about 50% of what is observed (see section 5d). Run 65 maintains a strong entrainment velocity, but the positive gradient of q is weakened considerably as the mixed layer moistens. The model is one-dimensional and therefore cannot account for the return flow and variations within it. It is possible that increasing values of q with decreasing radial distance are present, which could maintain the high latent heat fluxes at the top of the layer and yield a total en-

ergy input closer to what was diagnosed by the aircraft passes normal to the band.

Key parameters that affect the simulation are the entrainment velocity and the jump of θ_e across the top of the inflow layer. We can show how these parameters can lead to such a large increase in θ_e within the inflow with a few simplifying assumptions. If we assume that the entire inflow layer is like a convective mixed layer where buoyancy is the primary mechanism driving turbulence, then a conservation equation for θ_e, following the column is

$$Z_i \frac{d\bar{\theta}_e}{dt} = (\overline{w'\theta'_e})_s - (\overline{w'\theta'_e})_{zi}, \qquad (2)$$

where Z_i is the depth of the inflow layer. The surface fluxes $[(w'\theta'_e)_s]$ are approximated using the bulk aerodynamic equations. The flux of θ_e at the top of the inflow layer is estimated using an entrainment velocity and the gradient of θ_e found between the inflow layer and the outflow layer directly above:

$$(\overline{w'\theta'_e})_{Z_i} = -w_e(\bar{\theta}_{e,zi} - \bar{\theta}_{e,ml}). \qquad (3)$$

We can estimate an entrainment velocity by assuming that the height of the mixed layer is governed by the sum of the entrainment velocity w_e and the subsidence w_h (e.g., Stull 1988, 456–458):

$$\frac{dZ_i}{dt} = w_e + w_h. \qquad (4)$$

The V_R field derived from the Doppler suggests that the inflow layer does not change its height by more than a few hundred meters during the last 35-km radial distance covered; therefore we may assume as a first approximation that $w_e \sim w_h$. The in situ calculations estimate that the subsidence is nearly -0.15 m s^{-1}. If we assume that the return flow is saturated within 35 km of the band, then the jump of $\theta_e \sim +14$ K across the interface. This estimate is simply from the composite

TABLE 1. Summary of slab mixed-layer recovery model using modified HCO sounding.

		h (m)	S_v ($\times 10^{-3}$ J kg^{-1})	ΔS_v	θ_e (K)	q (g kg^{-1})	Δq
Initial Condition ($x = 0$)		800	305.0	2.0	345.5	15.0	3.0
Final Condition ($x = 90$ km)							
Run	Processes						
58	—	903	305.3	2.0	349.4	16.2	2.0
56	Rc	970	304.9	2.7	349.7	16.5	1.8
55	Sb	682	305.4	2.0	350.0	16.4	1.8
64	Sf	1079	305.3	2.6	350.4	16.6	2.0
65	Ro, Sb, Sf	927	305.0	3.1	351.1	16.8	1.8

Key: Ro—observed rainfall rate.
Rc—constant rainfall rate of 10 mm h^{-1}.
Sb—subsidence, $w = -0.15$ m s^{-1}.
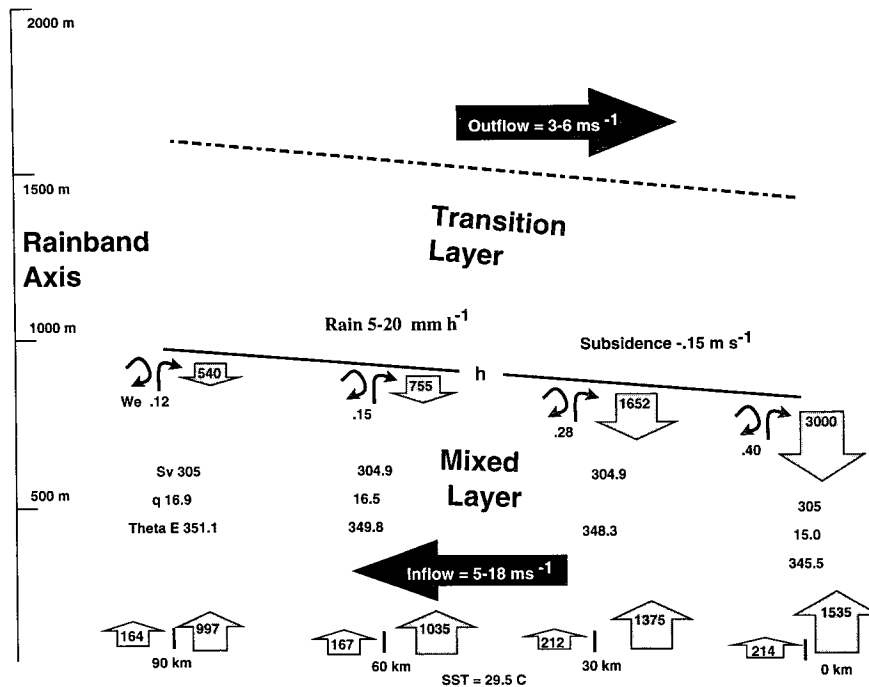Sf—fairall shear enhancement to entrainment velocity.

FIG. 20. Depiction of mixed layer growth and flux behavior at the surface and mixed layer top for General Structure Entrainment model run 65 (with shear, observed rain and subsidence) as described in Table 1. Horizontal scale at the bottom of the figure represents distance along the mixed-layer flow trajectory. Values of virtual dry static energy S_v, (10^3 J kg^{-1}), specific humidity q (g kg^{-1}), and θ_e (K) are displayed at 30-km intervals. Thick vertical arrows represent fluxes (W m^{-2}) with moisture fluxes (expressed as latent heat) shaded gray. Entrainment velocity (m s^{-1}) is represented as the bidirectional arrows.

sounding, but we have saturated the topmost layer. The dashed line in Fig. 19 shows what the value of θ_e would be if the layer above the inflow becomes saturated with no accompanying increase in temperature. If we use this jump in θ_e and the entrainment velocity that is equal to the subsidence, then the flux of θ_e through the top of the inflow would be nearly 2140 W m^{-2}. This flux, combined with the sensible and latent fluxes from the ocean surface, accounts for over 90% of the energy required to balance the budget for a column of inflow air.

6. Conclusions

a. Summary of results

On 12 September the two NOAA WP-3Ds concentrated on an intense rainband that was located 175 km from the circulation center and on the trailing side of Hurricane Gilbert. The in situ observations and the wind field derived from the pseudo-dual-Doppler scheme reveal that the band and its surrounding environment can be broken into three regions.

1) A high-reflectivity region (maximum dBZ > 45) with cellular structures exists that defines the major axis of the band. Convergence exceeds -3.0×10^{-3} s^{-1} as

the relative radial inflow decreases from -18 to 0 m s^{-1}. At an altitude of 2 km the radial inflow reverses, with a deep layer of radial outflow of 3–6 m s^{-1}. The vertical shear of the horizontal wind is in excess of 6.0 $\times 10^{-3}$ s^{-1} in the lowest 3 km. Updrafts are strong (5 to 7 m s^{-1}) in the subcloud and lower cloud layer, and downdrafts are weak (-2 to -3 m s^{-1}). Equivalent potential temperature changes are small in the downdrafts (2 to 3 K). Cold outflows are weak with the decrease of θ_v less than 1 K. The outflows are less than 800 m thick and cover only a few kilometers in the radial direction.

2) Inward of the band major axis there is weak reflectivity (0–15 dBZ). The flow is almost entirely tangential, and θ_e is nearly constant in the lowest kilometer for a radial distance of 30–40 km.

3) Outward of the band major axis exists a zone characterized by stratiform rain, decaying cells, and divergence. Relative radial inflow, with respect to the circulation center, increases from -8 to -18 m s^{-1}. This inflow is confined to the lowest 1.5 to 2.0 km above the sea. In this strengthening inflow the equivalent potential temperature increases markedly (7 K over 35-km radial distance). Wind speeds near the surface increase only slightly ($\sim$2 m s^{-1}) as the air approaches the band; sea surface temperature is nearly

constant at 29.2°C. The pressure decrease coincident with the increase of θ_e is inconsequential ($\sim$3 mb).

The estimated surface fluxes for the inflow, based on the bulk aerodynamic formulas with transfer coefficients that are assumed to increase with wind speed, cannot account for the rapid increase of θ_e in the inflow. Sensible heat flux is on the order of 100 W m^{-2} and latent heat flux is near 1000 W m^{-2}. The only way that the layer can be so rapidly energized is from entrainment of high θ_e from the layer directly above the inflow. This entrainment accounts for 50%–70% of the increase of θ_e in the inflow. Sounding data are sparse in this region, but what data are available support the existence of a layer of air emanating from either the rainband or the inner core of the vortex that has high θ_e values. Simulations that reduce the complicated inflow to a mixed layer emphasize the importance of this elevated source of high-θ_e air. The rate of entrainment and the lapse rate of θ_e are the key factors that control the rapid stoking up of the inflow layer. The simulations produce an increase of θ_e for the inflow column within a factor of 2 of what was observed.

b. Interpretation

The circulation of this rainband contrasts both other convectively active rainbands (Barnes et al. 1983; Powell 1990a) and squall lines (e.g. Zipser 1977; Gamache and Houze 1982) in that there is no inflow of dry air in the midlevels. This lack of midlevel inflow limits the production of evaporation-driven downdrafts and thus the production of cooler and drier outflows that could limit tropical cyclone intensity. For the Gilbert rainband the midlevel inflow is replaced by a deep layer of outflow originating from the band and inner core of the cyclone. The schematics in Fig. 21 highlight the differences between previously diagnosed convective bands [e.g., Hurricanes Earl (Powell 1990b) and Floyd (Barnes et al. 1983)] and the Gilbert rainband. The juxtaposition of an elevated layer of high θ_e, due

to low-level return outflow above the inflow, allows for the entrainment of this air back into the boundary layer. The more usual situation appears in Fig. 21b where subsidence below the anvil of the rainband (or squall line) places very dry air directly above the boundary layer; the entrainment of this air results in a minimum of θ_e appearing in the boundary layer hours after the convective-scale downdrafts that are associated with the high-reflectivity cells have reached the surface (e.g., Zipser 1977; Nicholls and Johnson 1984). In the Gilbert situation there exists surprising spatial variations of θ_e in the inflow that are intimately linked to the rainband circulation.

c. Speculation

1) THE ORGANIZATION OF THE FLUXES BY THE CONVECTION

Rotunno and Emanuel (1987) argue that it is the organization of the surface fluxes, and not the organization of the convection, that determines tropical cyclone intensification. This analysis demonstrates that there are regions within the tropical cyclone where there is a rapid increase of θ_e and other regions where little changes occur. These variations are largely a function of the circulations associated with mesoscale convective systems such as rainbands or the eyewall. The substantial modulation of the fluxes at the top as well as the base of the inflow by these MCSs is a vital aspect of tropical cyclone intensification that axisymmetric simulations cannot easily detect. Rainband location relative to the circulation center and the development of preferred inflow and outflow channels are significant factors that make the difference between a rainband enhancing or suppressing vortex intensification; it may also determine which bands deserve the label concentric ring. We hypothesize that MCSs within the hurricane vortex can organize the flux divergence of the inflow layer in such a way as to favor hurricane intensification.
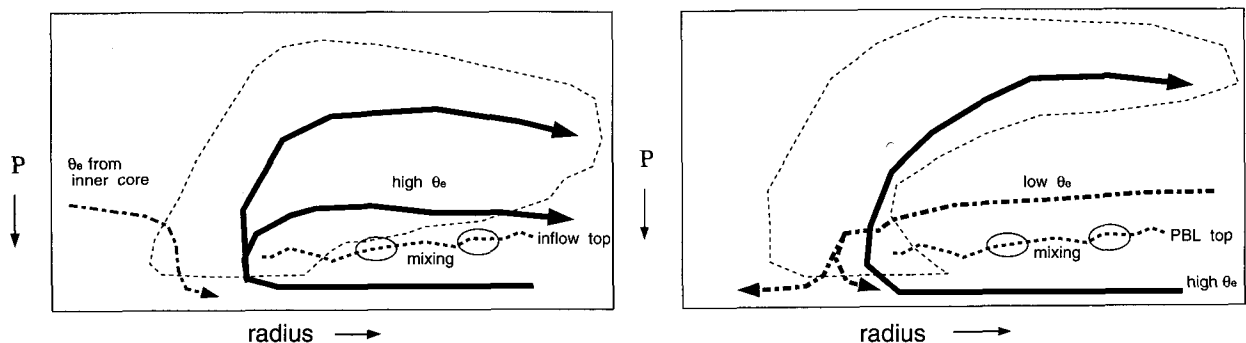

FIG. 21. (a) A schematic of the Gilbert rainband circulation. The dashed line delineates the top of the inflow and the bold arrows (solid for the primary updrafts, dash–dotted for the primary downdrafts) mark the primary circulation features. (b) A similar schematic, but for rainbands with midlevel inflow from greater radii (from Hurricanes Floyd and Earl).

2) THE PROBLEM WITH DEEP INFLOW

A deep inflow layer is commonly thought to be beneficial to tropical cyclone maintenance and intensity. Examination of the observations reveals that this is not necessarily so. Frank (1977a) built a composite view from many Pacific typhoons and shows that most of the inflow is below 850 mb. Jorgensen (1984) presented cross sections of the radial flow in Hurricane Allen (1980) and demonstrated that the inflow is also shallow for this intense storm (MSLP = 899 mb). The inflow to Gilbert is also constrained to a layer only 2 km deep. Under most environmental conditions, inflow above the subcloud and lower cloud layer is likely to be characterized by low-θ_e air that will serve as the source for downdrafts that will reduce the energy of the inflow and hence storm intensity.

3) APPLICATION OF THE GILBERT RAINBAND CIRCULATION TO THE EYEWALLS OF TROPICAL CYCLONES

Willoughby et al. (1989) classify Gilbert as a concentric system wherein rainbands propagate inward and evolve into a new eyewall. The rainband that we observe is like an eyewall, at least thermodynamically, in that we detect a rapid increase in the θ_e adjacent to the ring of convection. The θ_e radius–height cross sections for the better observed hurricanes such as Inez (Hawkins and Imbembo 1976) and Allen (Jorgensen 1984) manifest a rapid increase of θ_e within the inflow. Energy budgets for these inflow regions require prodigious amounts of heat and moisture that surface fluxes alone may not be able to account for, even with the large increases in wind speed near the eyewall. Other rainbands (e.g., Barnes et al. 1983; Barnes and Stossmeister 1986; Powell 1990a) do not exhibit this stoking-up quality, but these rainbands are not part of a concentric system. It is unfortunate that after this flight there are no data for 24 h that would show whether the Gilbert rainbands on the southwest side of the storm cease moving outward and contract. Both Yamasaki (1983) and Rosenthal (1980), in their simulations of a developing tropical cyclone with explicit convection, found bands that initially move outward, become stationary, then finally contract to form an eyewall.

d. Recommendations

The NOAA WP-3Ds have been recently equipped to make turbulent scale measurements during the TOGA COARE. We propose that a flux experiment be conducted just outward of an eyewall and on either side of a strong rainband. ODWs that are not compromised by liquid water would also be beneficial to ascertain the vertical thermodynamic structure in these environments efficiently. The application of a three-dimensional boundary layer model to the hurricane inflow problem would yield exciting results, especially when

coupled to the turbulent scale measurements that are now possible.

Much of the work concerning heat and moisture flux has been focused on the mixed layer. Usually this layer and the inflow layer are not coincident. We need to examine the entire layer that is heading toward the inner core to gain a more comprehensive understanding of tropical cyclone genesis and intensification.

REFERENCES

Anthes, R. A., and S. W. Chang, 1978: Response of the hurricane boundary layer to changes of sea surface temperature in a numerical model. *J. Atmos. Sci.,* **35,** 1240–1255.

Ball, F. K., 1960: Control of inversion height by surface heating. *Quart. J. Roy. Meteor. Soc.,* **86,** 483–494.

Barnes, G. M., and M. Garstang, 1982: Subcloud layer energetics of precipitating convection. *Mon. Wea. Rev.,* **102,** 102–117.

——, and K. Sieckman, 1984: The environment of fast- and slow-moving mesoscale convective cloud lines. *Mon. Wea. Rev.,* **112,** 1782–1794.

——, and G. J. Stossmeister, 1986: The structure and decay of a rainband in Hurricane Irene (1981). *Mon. Wea. Rev.,* **114,** 2590–2601.

——, G. D. Emmitt, B. Brummer, M. A. LeMone, and S. Nicholls, 1980: The structure of a fair weather boundary layer based on the results of several measurement strategies. *Mon. Wea. Rev.,* **108,** 349–364.

——, E. J. Zipser, D. P. Jorgensen, and F. D. Marks Jr., 1983: Mesoscale and convective structure of a hurricane rainband. *J. Atmos. Sci.,* **40,** 2125–2137.

——, J. F. Gamache, M. A. LeMone, and G. J. Stossmeister, 1991: A convective cell in a hurricane rainband. *Mon. Wea. Rev.,* **119,** 776–794.

Betts, A. K., and B. A. Albrecht, 1987: Conserved variable analysis of the convective boundary layer: Thermodynamic structure over the tropical oceans. *J. Atmos. Sci.,* **44,** 83–99.

——, and J. Simpson, 1987: Thermodynamic budget diagrams for the hurricane subcloud layer. *J. Atmos. Sci.,* **44,** 842–849.

Black, P. G., 1983: Ocean temperature changes induced by tropical cyclones. Ph.D. dissertation, Dept. of Meteorology, Pennsylvania State University, 278 pp.

Byers, H. R., 1944: *General Meteorology.* 2d ed. McGraw-Hill, 645 pp.

Carbone, R. E., F. I. Harris, P. H. Hildebrand, R. A. Kropfli, L. J. Miller, W. Moninger, R. G. Strauch, R. J. Doviak, K. W. Johnson, S. P. Nelson, P. S. Ray, and M. Gilet, 1980: The multiple Doppler Workshop, November 1979. *Bull. Amer. Meteor. Soc.,* **61,** 1169–1203.

Deardorff, J. W., 1979: Prediction of convective mixed-layer entrainment for realistic capping inversion structure. *J. Atmos. Sci.,* **36,** 424–436.

Emanuel, K. A., 1986: An air–sea interaction theory for tropical cyclones. Part I. Steady-state maintenance. *J. Atmos. Sci.,* **43,** 585–604.

Fairall, C. W., 1984: Wind shear enhancement of entrainment and refractive index structure parameter at the top of a turbulent mixed layer. *J. Atmos. Sci.*, **41**, 3471–3484.

Fankhauser, J. C., C. J. Biter, C. G. Mohr, and R. L. Vaughan, 1985: Objective analysis of constant altitude aircraft measurements in thunderstorm inflow regions. *J. Atmos. Oceanic Technol.*, **2**, 157–170.

Fitzjarrald, D. R., and M. Garstang, 1981: Boundary layer growth over the tropical ocean. *Mon. Wea. Rev.*, **109**, 1762–1772.

Frank, W. M., 1977a: The structure and energetics of the tropical cyclone. Part I: Storm structure. *Mon. Wea. Rev.*, **105**, 1119–1135.

——, 1977b: The structure and energetics of the tropical cyclone. Part II: Dynamics and energetics. *Mon. Wea. Rev.*, **105**, 1136–1150.

Gamache, J. F., and R. A. Houze Jr., 1982: Mesoscale air motions associated with a tropical squall line. *Mon. Wea. Rev.*, **110**, 118–135.

Hawkins, H. F., and S. M. Imbembo, 1976: The structure of a small, intense hurricane, Inez 1966. *Mon. Wea. Rev.*, **99**, 427–434.

Hildebrand, P. H., and C. K. Mueller, 1985: Evaluation of meteorological airborne Doppler radar. Part I: Dual-Doppler analyses of air motions. *J. Atmos. Oceanic Technol.*, **2**, 362–380.

Jordan, C. L., 1958: Mean soundings for the West Indies area. *J. Meteor.*, **15**, 91–97.

Jorgensen, D. P., 1984: Mesoscale and convective-scale characteristics of mature hurricanes. Part II: Inner core structure of Hurricane Allen (1980). *J. Atmos. Sci.*, **41**, 1287–1311.

——, P. H. Hildebrand, and C. L. Frush, 1983: Feasibility test of an airborne pulse-Doppler meteorological radar. *J. Climate Appl. Meteor.*, **22**, 744–757.

Large, W. G., and S. Pond, 1982: Sensible and latent heat flux measurements over the ocean. *J. Phys. Oceanogr.*, **12**, 464–482.

Lawrence, M. B., and J. M. Gross, 1989: Atlantic hurricane season of 1988. *Mon. Wea. Rev.*, **117**, 2248–2259.

LeMone, M. A., G. M. Barnes, and J. C. Fankhauser, 1988: Perturbation pressure fields measured by the aircraft around the cloudbase updraft of deep convective clouds. *Mon. Wea. Rev.*, **116**, 313–327.

Lilly, D. K., 1968: Models of cloud topped mixed layers under a strong inversion. *Quart. J. Roy. Meteor. Soc.*, **94**, 292–309.

Malkus, J. S., and H. Riehl, 1960: On the dynamics and energy transformation in steady-state hurricanes. *Tellus*, **12**, 1–20.

Marks, F. D., Jr., and R. A. Houze Jr., 1984: Airborne Doppler radar observations in Hurricane Debby. *Bull. Amer. Meteor. Soc.*, **65**, 569–582.

——, and ——, 1987: Inner core structure of Hurricane Alicia from airborne Doppler observations. *J. Atmos. Sci.*, **44**, 1296–1317.

——, and H. A. Friedman, 1994: The 1994 Hurricane Field Program Plan. NOAA/AOML/HRD, Miami, FL, 131 pp.

McCaul, E. W., 1991: Buoyancy and shear characteristics of hurricane-tornado environments. *Mon. Wea. Rev.*, **118**, 1954–1978.

Nicholls, M. E., and R. H. Johnson, 1984: A model of a tropical squall line boundary layer wake. *J. Atmos. Sci.*, **41**, 2774–2792.

Ooyama, K., 1969: Numerical simulation of the life cycle of tropical cyclones. *J. Atmos. Sci.*, **26**, 3–40.

Paluch, I. R., 1979: The entrainment mechanisms in Colorado cumuli. *J. Atmos. Sci.*, **36**, 2467–2478.

Powell, M. D., 1987: Changes in the low-level kinematic and thermodynamic structure of Hurricane Alicia (1983) at landfall. *Mon. Wea. Rev.*, **115**, 75–99.

——, 1990a: Boundary layer structure and dynamics in outer hurricane rainbands. Part I: Mesoscale rainfall and kinematic structure. *Mon. Wea. Rev.*, **118**, 891–917.

——, 1990b: Boundary layer structure and dynamics in outer hurricane rainbands. Part II. Downdraft modification and mixed layer recovery. *Mon. Wea. Rev.*, **118**, 918–938.

Rodgers, D. P., 1989: The marine boundary layer in the vicinity of an ocean front. *J. Atmos. Sci.*, **46**, 2044–2062.

Rosenthal, S., 1980: Numerical simulation of tropical cyclone development with latent heat release by the resolvable scales. Part II: Propagating small scale features seen in the prehurricane phase. NOAA Tech. Rep. ERL413-AOML 29, 43 pp.

Rotunno, R., and K. A. Emanuel, 1987: An air–sea interaction theory for tropical cyclones. Part II: Evolutionary study using a nonhydrostatic numerical model. *J. Atmos. Sci.*, **44**, 542–561.

——, J. B. Klemp, and M. L. Weisman, 1988: A theory for strong, long-lived squall lines. *J. Atmos. Sci.*, **45**, 463–485.

Shay, L. K., R. L. Elsberry, and P. G. Black, 1988: Vertical structure of the ocean current response to hurricanes. *J. Phys. Oceanogr.*, **19**, 649–669.

Stull, R. B., 1988: *An Introduction to Boundary Layer Meteorology.* Kluwer, 666 pp.

Thorpe, A. M., M. J. Miller, and M. W. Moncrieff, 1982: Two-dimensional convection in nonconstant shear: A model of midlatitude squall lines. *Quart. J. Roy. Meteor. Soc.*, **108**, 739–762.

Wakimoto, R. M., 1982: The life cycle of thunderstorm gust fronts as viewed with Doppler radar and rawinsonde data. *Mon. Wea. Rev.*, **110**, 1060–1082.

Weisman, M. L., J. B. Klemp, and R. Rotunno, 1988: Structure and evolution of numerically simulated squall lines. *J. Atmos. Sci.*, **45**, 1990–2013.

Willoughby, H. E., J. M. Masters, and C. W. Landsea, 1989: Hurricane Gilbert: A record minimum surface pressure for the Western Hemisphere. *Mon. Wea. Rev.*, **117**, 2824–2828.

Yamasaki, M., 1983: A further study of the tropical cyclone without parameterizing the effects of cumulus convection. *Pap. Meteor. Geophys.*, **34**, 221–260.

Zipser, E. J., 1977: Mesoscale and convective-scale downdrafts as distinct components of squall line circulation. *Mon. Wea. Rev.*, **105**, 1568–1589.

——, R. J. Meitin, and M. A. LeMone, 1981: Mesoscale motion fields associated with a slowly moving GATE convective band. *J. Atmos. Sci.*, **38**, 1725–1750.